Influence of Temperature-Dependent Specific Heat and Conductivity on Heat and Gas Migration in Rock Salt:

A Computational Study within BATS II

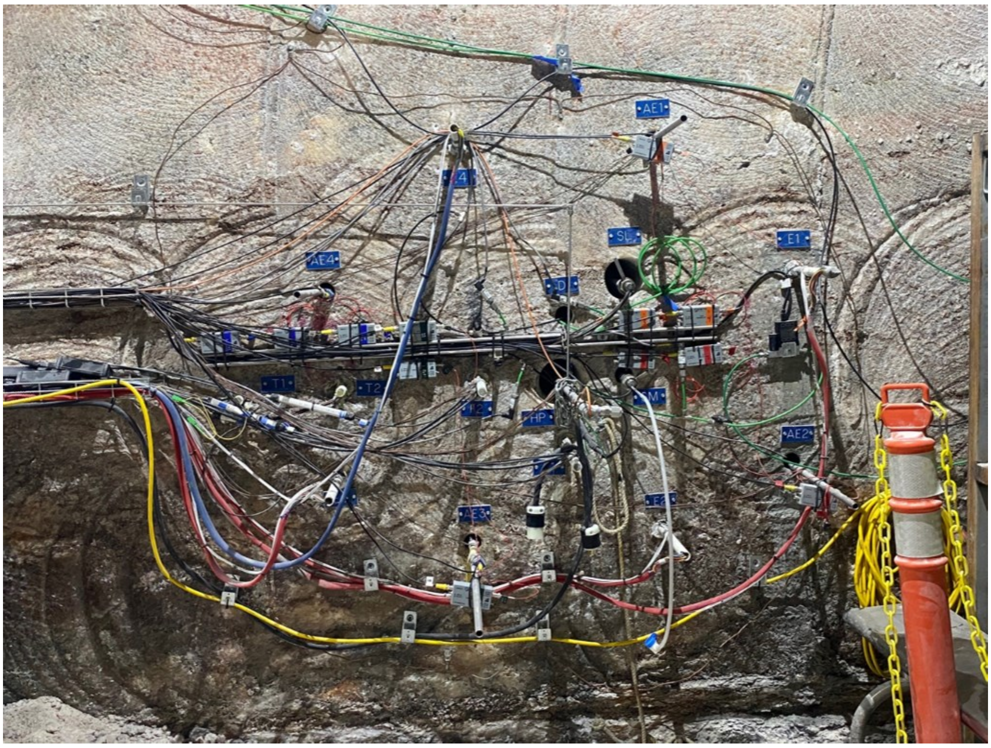

MSc Internship Report by Tijmen Ottenheim (6574084)

Department of Earth Sciences, Utrecht University, Netherlands

Internship conducted at Covra, Netherlands

Internship supervisors:

Dr. Jeroen Bartol (Covra) and Dr. Fred Beekman (UU)

February 2025

Summary

The safe disposal of radioactive waste in geological formations requires a detailed understanding of thermal and gas migration processes in rock salt. Rock salt is a key candidate for underground waste storage due to its low permeability and self-sealing properties. This study, part of the BATS II project within DECOVALEX, investigates two key aspects: (1) the effect of non-linear thermal parameters (specific heat capacity and thermal conductivity) on heat conduction in rock salt and (2) gas migration between two boreholes within the same rock salt body. A numerical modeling approach was employed using COMSOL Multiphysics to simulate experimental data from the Waste Isolation Pilot Plant (WIPP) site, aiming to improve the understanding of subsurface processes relevant to nuclear waste disposal. The study incorporated temperature-dependent material properties to assess their influence on heat transport and evaluated gas migration patterns through the rock salt.

The results indicate that thermal conductivity and specific heat capacity play a significant role in the heat distribution within rock salt, affecting the temperature gradients. The mathematic equation for both parameters are very specific for the rock samples, small changes result in significant changes in the steady-state temperatures of each sensor. The heating and cooling rates predicted by the computational results are faster than the rates observed at the WIPP experimental site.

The findings in the study contribute to the ongoing assessment of rock salt as a host rock for radioactive waste storage by improving predictive models for long-term repository behavior. The study highlights the necessity of accounting for coupled thermal-hydrological-mechanical (THM) interactions in safety assessments. Future research will focus on refining the mechanical deformation effects, integrating experimental validation, and extending the modeling approach to account for long-term creep behavior and stress-induced changes in permeability.

Table of Contents

Summary ... 2
1. Introduction ... 5
2. Background ... 7
   2.1. Historical Overview ... 7
   2.2. COPERA Research Program ... 7
3. Model Setup ... 9
   3.1. Setup of Thermal Model ... 9
      3.1.1. Geometry ... 10
      3.1.2. Boundary Conditions ... 11
      3.1.3. Simulation Set-Up Thermal Models ... 12
   3.2. Setup of Hydrological Model ... 12
      3.2.1. Geometry ... 12
      3.2.2. Boundary Conditions ... 13
      3.2.3. Simulation Set-Up Hydrological model ... 13
   3.3. Material Properties Thermal/Hydrological Model ... 14
4. Model Results ... 15
   4.1. Results of Step 0 Thermal Models ... 15
   4.2. Parametric Studies of Step 0 Thermal Models ... 18
   4.3. Convergency Studies of Step 0 Thermal Models ... 18
   4.4. Sensitivity Analysis of Step 0 Thermal Models ... 19
   4.5. Results of Step 1 Thermal Model ... 25
   4.6. Results of Step 1 Hydrological Model ... 27
   4.7. Parametric Studies of Step 1 Hydrological Model ... 28
   4.8. Convergency Studies of Step 1 Hydrological Model ... 29
   4.9. Sensitivity Analysis of Step 1 Hydrological Model ... 30
5. Discussion ... 32
   5.1. Temperature-Dependent Specific Heat Capacity and Thermal Conductivity ... 32
   5.2. Homogeneity Versus Heterogeneity in the Thermal Models ... 33
   5.3. Sensor F1's Deviation Between Experiment and Model ... 34
   5.4. Single-Phase Flow in the Hydrological Model ... 34
   5.5. Storage Coefficient Dependency ... 35
   5.6. Influence of Temperature Increase on Gas Migration ... 36
   5.7. Uncertainty in the Computational Models ... 36
Conclusion ... 37
Acknowledgments ... 37

References 38
Appendices 40
Appendix 1 40
Appendix 2 40
Appendix 3 41
Appendix 4 41
Appendix 5 42
Appendix 6 43
Appendix 7 43

1. Introduction

Nuclear energy is an important component of the global energy mix, accounting for approximately 9% of the world's electricity production (Energy Agency, 2025). Its role has become increasingly critical as nations strive to achieve energy security while reducing greenhouse gas emissions. Unlike fossil fuels, nuclear power plants generate electricity through fission reactions without emitting carbon dioxide during operation, making it a low-carbon energy source (Bodansky, 2007). Globally, there are over 440 operational nuclear reactors spread across 30 countries, with the United States, France, and China leading in capacity (Schneider et al., 2025). To meet growing (sustainably) energy demands many countries, the governments of countries such as China and India are expanding on the number of nuclear energy facilities in their countries (Gao et al., 2024). Meanwhile, nations like Germany and Belgium are phasing out nuclear power due to policy decisions and public concerns about safety and waste management (Gutting et al., 2024).

In the Netherlands, nuclear energy has played a modest but steady role in the energy mix. The country operates a single commercial nuclear power plant in Borssele, which contributes approximately 3% of the national electricity supply (Schneider et al., 2025). Historically, the Dutch approach to nuclear energy has been cautious, influenced by public opinion and concerns over waste disposal (Schneider et al., 2025). However, recent shifts in energy policy reflect a growing recognition of nuclear power as a vital tool in achieving climate goals. The Dutch government has announced plans to construct four additional nuclear reactors by 2035 to reduce reliance on fossil fuels and support the transition to a sustainable energy system (Dutch Government, 2024). Besides the nuclear energy reactor located in Borssele, the Netherlands have two other nuclear reactors. One of these reactors is located in Petten and produces medical isotopes that are used worldwide for diagnosing and treating cancer and other illnesses, while the other is located at the University of Delft and is used for research purposes (COVRA, 2024). Along with medical facilities, also industrial companies are responsible for the production of radioactive waste.

Currently, all radioactive waste that was and is produced in the Netherlands is stored in the storage facility of COVRA (Centrale Organisatie Voor Radioactief Afval) in Nieuwdorp (Zeeland). The storage of radioactive waste at COVRA is not a long-term solution for the problem, since a part of the waste will still be radioactive after one thousand years of storage (COVRA, 2024). A permanent deep geological disposal is one of the solutions to ensure that the radioactive waste will remain out of the human living environment. The current policy stands that the Geological Disposal Facility (GDF) must be operational by 2130 (Berkers et al., 2024). The Dutch subsurface has two lithologically-determined geological environments that may be suitable for hosting a long term disposal facility, rock salt and clay formations. The different research programs in the past focused on these two types of host rocks, with rock salt being an interesting option due to the presence in the subsurface.

Research on rock salt as a suitor for disposal of radioactive waste has been done by different countries. The earliest research programs started in the fifties and were done independently, initial collaborations were limited, with each country focusing on national programs and testing at local sites. In the eighties, the OECD Nuclear Energy Agency (NEA) and the International Atomic Energy Agency (IAEA) facilitated early discussions on geological disposal. Eventually resulting in the establishment of the DECOVALEX (Development of Coupled Models and their Validation against Experiments) program in the mid-nineties. The international research program focusses on enhancing the effects of radioactive waste on rock, COVRA is one of the participating institutes. DECOVALEX is an international collaborative project designed to improve understanding of coupled thermal, hydraulic, mechanical, and chemical (THMC) processes in geological systems (Birkholzer et al., 2019). The Brine Availability Test in Salt task

(BATS II), part of the DECOVALEX program, is the continuation of Task E from the previous project cycle and aims to simulate observed thermal-hydrogeological and mechanical (THM) responses due to heating as observed in boreholes in bedded salt at Waste Isolation Pilot Plant (WIPP) near Carlsbad, New Mexico (USA). The BATS II task is divided into five smaller steps, building up in scope and complexity. The five step are listed below:

Step 0: Modeling the heat conduction during three equal-length tests at three different power levels (200 W, 400 W and 500 W), matching experimental data from experiments held at the WIPP.

Step 1: Modeling pressure decrease due to gas migration between boreholes under both ambient and heated conditions, matching experimental data from experiments held at the WIPP.

Step 2: Including the effects of one or more salt-specific brine sources in numerical models (fluid inclusions and saturated clay).

Step 3: Modeling brine production during two different length heater tests (5 weeks and 8 weeks) at the same power level.

Step 4: Scaling up BATS2 results to repository-scale relevance (cross-collaboration with Salt PA task), including drift-scale EDZ (excavation damaged zone) migration of brine, which may be an initial condition for PA models.

The objective of this study is to complete step 0 and step 1 using the COMSOL Multiphysics modelling software. The insights obtained with the modeling assignments from the BATS II task, will help optimization of the GDF design that can be constructed in the Dutch subsurface.

2. Background

The safe and sustainable disposal of long-term radioactive waste remains a significant challenge for many countries, including the Netherlands. The safe and sustainable disposal of long-term (>100,000 yrs) radioactive waste remains a significant challenge for many countries, including the Netherlands. The problem is the limited storage space and the uncertainty regarding developments over the next 100 years. Deep geological disposal is not affected by surface events such as war or global warming. The Dutch governments had initiated several research programs to investigated the possibilities in the Dutch subsoil (Verhoef et al., 2020).

2.1. Historical Overview

Dutch research into a GDF has focused on two different types of rocks: rock salt and poorly indurated clay. Rock salt as the host rock has been spanning five different research programs over a period of more than 50 years (Figure 1). The programs have been separated by a few years, resulting in weakening of the research infrastructure while earlier collected knowledge had to be recovered at the start of a new research program.

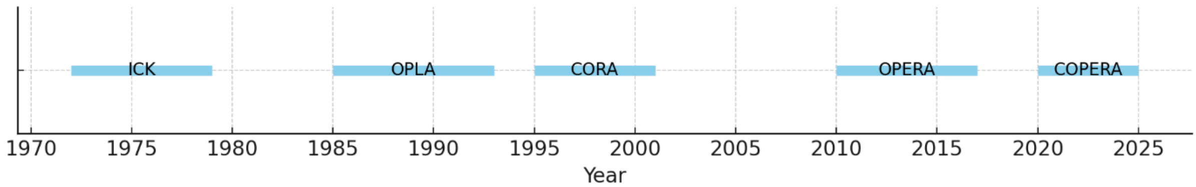

Figure 1: Timeline of Dutch GDF projects considering (partially) rock salt as an option as host rock. Based on Bartol & Vuorio (2022) and Verhoef et al. (2020).

The Netherlands has conducted several research programs on geological disposal of radioactive waste. The Interdepartementale Commissie Kernenergie (ICK) (1972–1979) laid the groundwork by identifying Zechstein rock salt formations as promising disposal sites (Verhoef et al., 2020; Bartol & Vuorio, 2022). This was followed by the Onderzoekprogramma Lange Afvalopslag (OPLA) (1985–1993), which expanded on ICK's findings through detailed studies on long-term storage and disposal feasibility in salt formations. The Commissie Opberging Radioactief Afval (CORA) (1995–2001) broadened the scope to include clay as a potential host rock and analyzed socio-political, ethical, and technical aspects of disposal (Commissie Opberging Radioactief Afval, 2001). The final program, Onderzoeksprogramma Eindberging Radioactief Afval (OPERA) (2011–2018), developed a safety case for geological disposal, focusing on clay formations and a disposal concept for projected waste inventories in 2130 (Verhoef et al., 2020). OPERA confirmed that clay formations are a viable option for long-term radioactive waste disposal in the Netherlands.

2.2. COPERA Research Program

The COPERA research program, which started in 2020, is the ongoing research program and successor of the OPERA program, focusing on the continuation of research into geological disposal as a long-term solution. The program aims to expand on the knowledge base established by OPERA, to develop a disposal concept in rock salt and to ensure readiness for decision-making processes in 2130 (Verhoef et al., 2020). This research program is part of an extended long-term program, which continues up to at least 2050. This long-term research program aims to strengthen the national research infrastructure and enable Dutch researchers to participate in international knowledge platforms, like the DECOVALEX project. This program focusses on poorly indurated clays as well as rock salt in the subsoil, while taking into account both the begin and end of the radioactive waste chain. Initiating a research program now, despite the final disposal facility only being needed in approximately 100 years, allows for the opportunity to learn from international experiences and advancements in geological disposal. Research developments abroad in countries like Finland and Sweden, show the importance to stay connected and learn from these experienced countries. These two Scandinavian countries that already started with the construction of their final disposal facilities

The participation of COVRA in the DECOVALEX program is one of the advantages for the Dutch research program. The DECOVALEX program was established in 1992, and brings together leading researchers and organizations to tackle complex subsurface challenges relevant to radioactive waste disposal, geothermal energy, and other geoscience fields. The program is structured around several tasks, each addressing a specific research focus. Through benchmarking exercises and collaborative modeling efforts, DECOVALEX enhances the predictive capabilities of coupled-process simulations, providing a foundation for safer and more effective subsurface engineering applications like a repository. The program consists of phases that last four years, the current and ninth project phase started in 2024 and ends in 2027. The BATS II task (as part of the DECOVALEX program) is especially focusing on the material properties of the excavation damaged zone (EDZ) (Figure 2) and its evolution over time. The EDZ is a halo of higher-permeability, higher-porosity, and reduced brine saturation compared to the far-field that surrounds excavations in the underground (Kuhlman et al., 2023a).

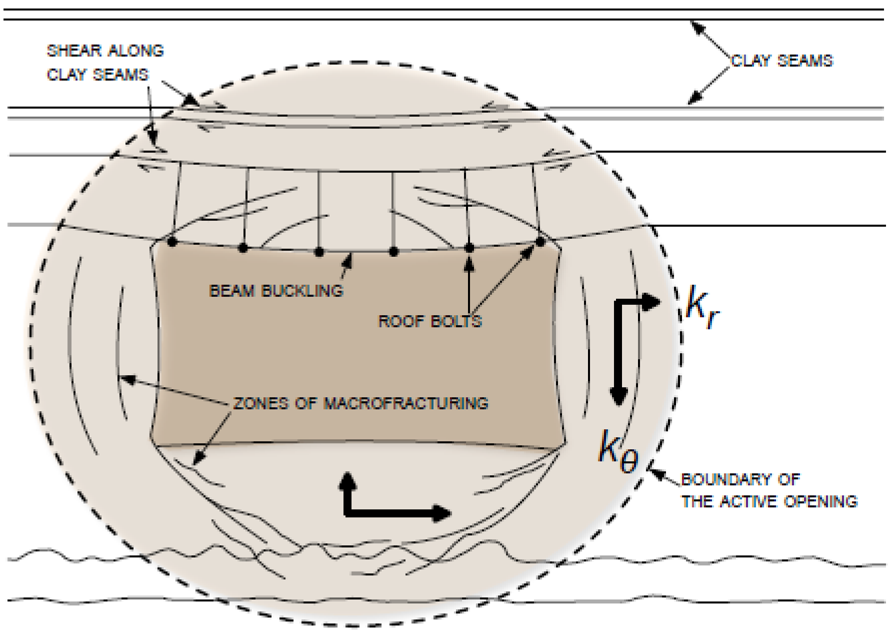

Figure 2: Cross-section view of excavation damaged zone (EDZ). After Borns & Stormont (1988.).

3. Model Setup

To numerically simulate the experiments that were held at the WIPP in Carlsbad (New Mexico, USA), the COMSOL Multiphysics version 6.2 software was used. COMSOL Multiphysics is a finite element-based software platform for modeling and solving coupled multiphysics problems. COMSOL allows for the integration of various physical phenomena, such as heat transfer, fluid dynamics, and structural mechanics, using a combination of finite element and finite difference methods. Mesh refinement and adaptive solvers were employed to achieve convergence and improve solution accuracy. Two thermal models and one hydrological model were created, each serving their own purpose and goal in answering the questions from step 0 and 1.

The experimental setup used for the experiments in the WIPP is as follows. In a horizontal borehole within rock salt, a controlled thermal source is installed, referred to as the heater. Surrounding this borehole, five parallel boreholes are equipped with temperature sensors. These sensors are aligned in a plane perpendicular to the borehole containing the heat source, with a constant spacing between boreholes, ensuring a linear increase in distance from the source. During the experiment, the heat source is activated for a specific period, causing the generated heat to propagate radially outward. Each of the five sensors records the local temperature increase for a set period of time capturing the heating and cooling of the host rock. Each sensor generates a temperature-time curve. The experiment is repeated multiple times with varying power levels. By analyzing differences between the recorded temperature-time curves, the experiment aims to provide insight into the relative influence of different thermal properties of rock salt on the magnitude and rate of conductive heat transfer from a heat source, analogous to radioactive waste. A picture of the experimental setup at the WIPP can be seen on the frontpage of this report.

3.1. Setup of Thermal Model

Step 0 aims to deepen the understanding of the effects of temperature-dependent non-linearities in rock salt, so a temperature-dependent specific heat and thermal conductivity are needed. Additionally, the next step of the BATS II has a heat transfer component, combined with a hydrological component. The COMSOL Heat Transfer in Solids Module was used to simulate thermal conduction in rock salt, governed by Fourier's law [Eq 1.], where ρ is density, c_p is the specific heat capacity, k is thermal conductivity, T is temperature and Q is the heat source term.

$$\rho c_p \frac{\partial T}{\partial t} = \nabla \cdot (k \nabla T) + Q \qquad \text{[Equation 1]}$$

The equation accounts for the balance of thermal energy due to conduction, heat generation and energy storage (heating) in the medium. The Finite Element Method (FEM) is used to calculate the temperature at different locations within the rock body. The Finite Element Method (FEM) in COMSOL divides the geometry into small, discrete elements (the mesh) and solves partial differential equations (PDEs) within each element using numerical approximations.

The experimental data from the WIPP site were obtained with the use of six different thermocouples that recorded the temperature during the runtime of the experiment. For the experiment at step 0, three heating phases were included in the experiment, step 1 included only one heating phase. Five of the six sensors were located on the same plane as the center of the heater (2.972 meter behind the drift wall plane), the other sensor was located at a depth of 4.572 meter (also see Fig. 3).

3.1.1. Geometry

The model is a two-dimensional axis-symmetrical model. Such axis-symmetrical two-dimensional model is suitable because heat will radiate in all directions, only the distance maters for the calculations in this model. In a one-dimensional model this will be reduced to only one direction, resulting in overestimate when comparing the experimental outcomes. Additionally, this approach is computational less demanding than a three-dimensional model. The domain consists of a square representing the rock salt, with the side of the square having a length of 20.0 meter. This length was adopted because a smaller length of 15.0 meter would result in heating at the boundaries of the domain, influencing the calculated temperatures at the locations of the sensors, whereas a domain with a length larger than 20 meter would increase the computational time required. Therefore, 20.0 meter was used as a numerically efficient domain length.

The sensors are set into place in the boreholes with grout. Because of the minimal amount of grout between the heater and sensor (nine millimeters), its thermal perturbing effect is expected to be negligible and the material is left out of the model.

The heater borehole is also included in the model as a subtraction of the square of the host rock. The other boreholes, in which the thermocouples are located, are not subtracted, due to the two-dimensional axis-symmetrical nature of the model the boreholes would interfere with the thermal convection in the model. The dimensions of the boreholes and sensors are included in a table in the Appendix (Appendix 1 and 2), and the locations of the boreholes (as seen from the drift, side and top view) are shown in Figure 3.

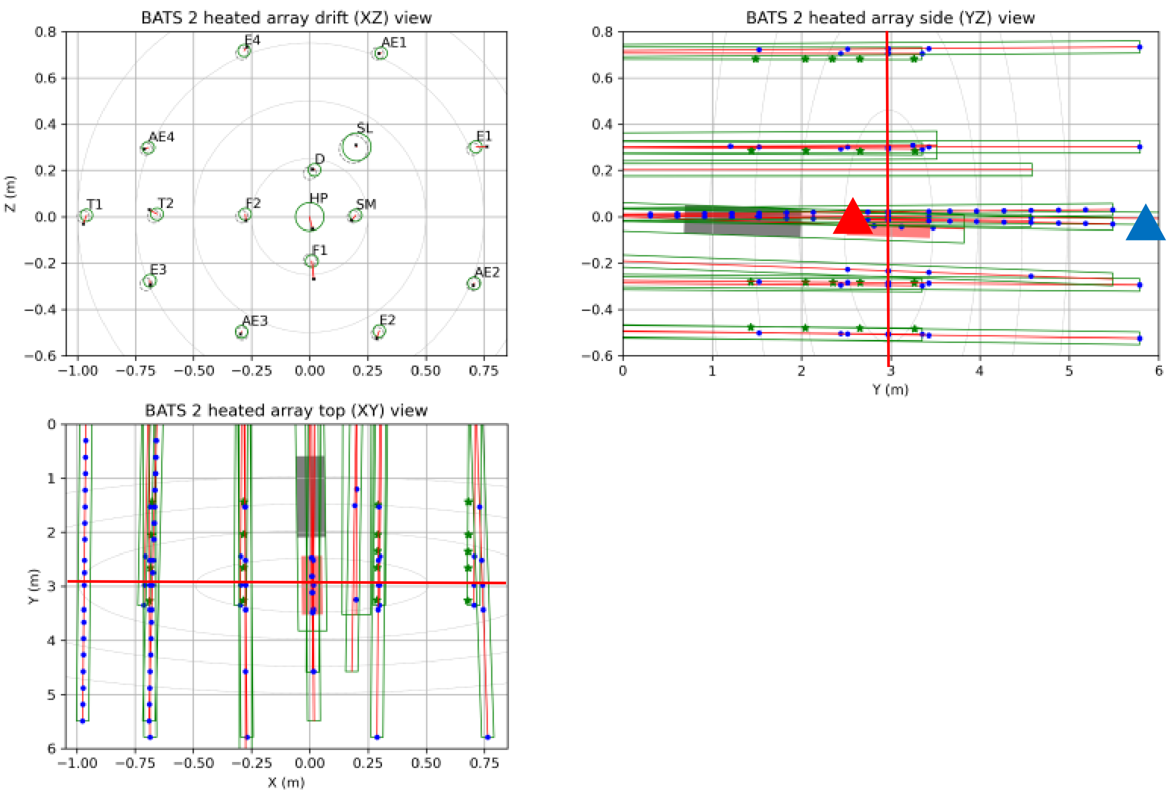

Figure 3: From (Kuhlman et al., 2024), the drift, side and top view of the boreholes used in the BATS II experimental setup. The heater is located at XZ- coordinates (0,0), with the center located at 2.972 m depth. Five sensors (F1, F2, E2, T1a and T2) are located in the same plane was the center of the heater (red line in the top and side view projection), T1b is at the end of borehole T1. The red triangle is the sample location of H-HP_2.5 and the blue triangle is the sample location of U-HP_6.4-6.25.

The sensors are used to record the temperature during the experiment. They are built into the model as points. The coordinates of these points originate from the experimental set-up from the DECOVALEX program. The conceptual model is shown in Figure 4.

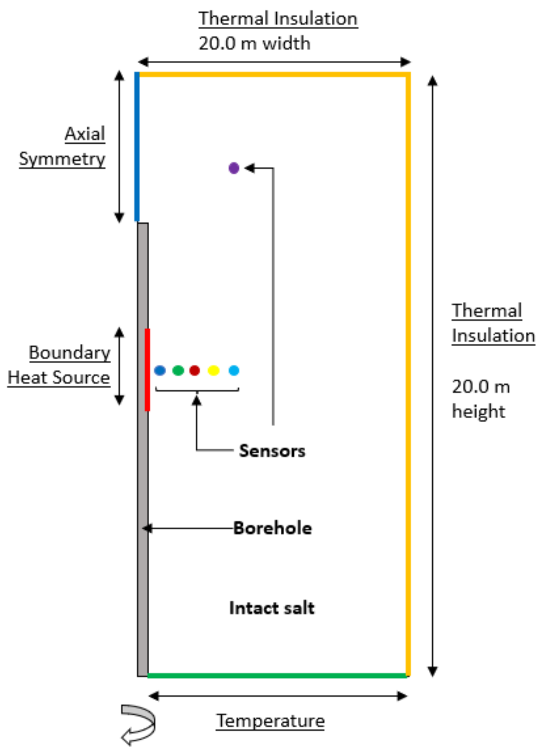

Figure 4: Conceptual, axisymmetrical, two-dimensional model for calculations of temperature using the Heat Transfer in Solids Module in COMSOL Multiphysiscs. Note that the proportions in the model are not accruate for this concept. Dark blue is sensor F1; Green is sensor F2; Red is E2; Yellow is T2; Light blue is T1a; Purple is T1b.

3.1.2. Boundary Conditions

A variable heat flux was applied to the heater surface (red line). To ensure the heater's power output was accurate, the data that was used consisted of the recorded measured power from the heater during the experiment conducted at the WIPP. With earlier experiments (Kuhlman et al., 2023b) showing that efficiency of the heater was 93.0%, the heater output was multiplied with 0.93. Note that step 0 and step 1 had different heater power input, both came from the data provided by the BATS II group (Appendix 3 and 4) .

At the WIPP, the dimensions of the host rock significantly exceed the 20-meter scale utilized in the COMSOL model. To prevent the boundaries heat leaving the model, thermal insulation was applied to the right and upper boundaries (yellow lines).

The ambient temperature at the WIPP was measured at 27.8 °C at the start of the experiments that were simulations of step 0. For step 1 the initial temperature was measured at 28.0. These temperatures were used as the initial temperature throughout the domain. Due to seasonal temperature changes within the WIPP a linear temperature boundary condition has been imposed to the drift face, with an ambient temperature difference of ≤ 2 °C between summer and winter. This condition is applied to the green colored boundary in Figure 4 .

3.1.3. Simulation Set-Up Thermal Models

An unstructured tetrahedral mesh was used for the model calculations, with finer elements near the heat source. The total number of elements was 102,364 (millimeter scale). For the calculation of the model a time-dependent study was employed to simulate heat transfer over time. The BDF (backward differentiation formula) method was applied for transient analysis with a strict time-stepping to balance accuracy and computational efficiency. The BDF is a numerical technique used for solving stiff ordinary differential equations and partial differential equations in time-dependent analyses. It is an implicit, multi-step method that approximates time derivatives using backward finite differences. The simulation for step 0 simulated 3.000 hours with a maximum time step of 10 hours. The thermal simulation for step 1 simulated 1728 hours with a maximum time step of 5 hours. Convergence was ensured with a relative tolerance of $1e^{-3}$ and an absolute tolerance of $1e^{-1}$. The solver monitored residuals to confirm solution stability at each time step.

3.2. Setup of Hydrological Model

The Darcy's Law interface in COMSOL Multiphysics 6.2 is designed for simulating fluid flow through porous media, utilizing Darcy's law to describe the relationship between the fluid velocity, pressure gradient, and the properties of the porous medium. The governing equation of Darcy's law is given by Equation 2, the porous medium is governed by the equation given by Equation 3 (combined with the continuation equation).

$$u = -\frac{k}{\mu} * \nabla \mathrm{P} \quad \text{[Equation 2]}$$

$$\rho * S_P \frac{\delta p}{\delta t} + \nabla * (\rho * u) = Q_m \quad \text{[Equation 3]}$$

With u is the specific discharge (volumetric flow rate per unit area, k is the permeability of the porous medium, μ is the dynamic viscosity of the fluid, S_P is the storage coefficient and P is the pressure. With Q representing a source or sink term, such as fluid injection of extraction. The Darcy's Law interface assumed single-phase flow by default, this means that the fluid occupying the porous medium is considered to have a single composition (e.g. a liquid like water or brine, or a gas like steam or argon) and doesn't change phase (liquid to gas or vice versa). By using the properties (dynamic viscosity and density) of argon and assuming an incompressible gas, the Darcy module becomes valid to use for gas transport through the porous medium.

Boundary conditions such as prescribed pressure and no inflow or outflow (impermeable) can be specified. Initial conditions for pressure distribution can also be applied to align the simulation with the experimental states. The inlet had an initial pressure of 20.3 psi, while the outlet and host rock had an initial pressure of 0.0 psi.

The experimental data from the WIPP site had been obtained with the use in inlet that was filled with argon gas before the experiment started. The pressure dropped quickly, with the observation that the gas broke through to the HP borehole. Flowrate of N_2 through the HP borehole was used to sample the argon that was found in the sink; the flow was nominally 100 mL/min during the whole test.

3.2.1. Geometry

To simulate the flow of argon gas from inlet to outlet a two-dimensional model was created, with the source (D) and sink (HP) borehole both included with the diameters from Appendix 1. The domain consist of a rectangle representing the rock salt, with a width of 35.0 cm and a height of 20.0 cm. The distance between the centers of both boreholes was set to 20.3 cm.

During the analysis of the experimental results from the WIPP, i.e. the data that is aimed to be match with the model results, it was noticed that most of the argon gas was collected at the source. Around 93% of the argon was collected, which could explained only by the presence of a fracture or a network of fractures. Therefore, a rectangular zone with an increased permeability was created between the two boreholes in the model, representing the fracture located between the argon source and sink. Using BATS2 data, the permeability of this fracture was set at $3.8*10^{-14}$ m^2. The aperture of the fracture is of importance due to the trends that can be seen in the provided data: during the heating no gas migrates through the host rock. This would result in one fracture with a maximum aperture of 1.004 µm, connecting the source and the sink (see appendix for calculation)

Another parameter that must be considered is the storage coefficient (S_P). This parameter can be quantified by different types of storage model; from density and porosity, linearized storage, poroelastic storage, quasistatic or user specified. For this model the storage coefficient is specified at $10^{-6.73}$ Pa^{-1}.

3.2.2. Boundary Conditions

To replicate the pressure difference between the inlet and the rest of the system, an initial pressure of 20.1 psi was assigned to the inlet, while the rest of the model was set to an initial pressure of 0 psi. A no-flow boundary condition was applied to the edges of the rock (red lines, Fig. 5).

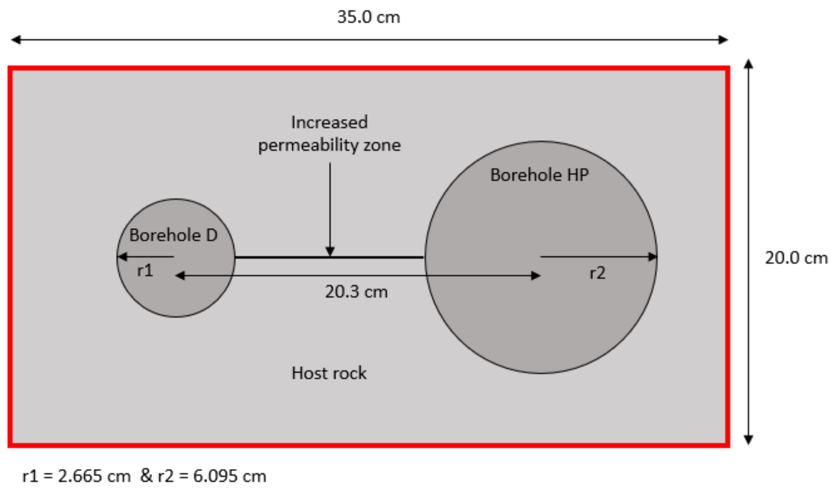

Figure 5: Conceptual, two-dimensional, hydrological model for pressure calculations using the Darcy's Law Module in COMSOL Multiphysics. The red-colored boundaries have a no-flow condition. Borehole D has an initial pressure of 20.3 psi and borehole HP as well as the host rock had an initial pressure of 0 psi.

3.2.3. Simulation Set-Up Hydrological model

An unstructured tetrahedral mesh was used for the model calculations, with finer elements near and in the fracture and boreholes. The total number of elements was 13554 (centimeter scale) For the calculation of the model a time-dependent study was employed to simulate pressure changes over time. The BDF method was applied for transient analysis with a strict time-stepping to balance accuracy and computational efficiency.

The simulation modelled 96 hours with a maximum time step of 0.2 hours. Convergence was ensured with a relative tolerance of $1e^{-3}$ and an absolute tolerance of $1e^{-1}$.

3.3. Material Properties Thermal/Hydrological Model

The host rock's mineralogy was considered homogeneous across the entire domain, thus with uniform material properties throughout. The calculations for thermal models required the density of rock salt, specific heat capacity and thermal conductivity as material properties. Research data from earlier experiments on rock samples from the WIPP was used to find temperature-dependency of the thermal conductivity and specific heat capacity parameters. The outcome of these experiments is visualized in the two graphs included in the Appendix 5 & 6..

The temperature-dependent formula for specific heat capacity can be derived from various rock samples taken at different locations. However, because data of the H-HP_2.5 sample was collected in close proximity to the heater and sensors (see location of the red triangle in Figure 2), that data was used to determine the trendline formula. This formula, shown in the table below with its corresponding R^2 (Table 1), is characterized by a polynomial fit. Experiments on the thermal conductivity of the rock samples showed a temperature-dependency, similarly to the specific heat capacity. A logarithmic fit gives the best R^2-value and is the formula that was used for the temperature dependency of the host rock in the model. All properties are shown in Table 1.

The calculations for the hydrological model required the following material properties: the density of the gas (Argon), dynamic viscosity of the gas, porosity and permeability of the host rock. These properties are included in Table 1.

Table 1: All material properties used for the calculations in the thermal and hydrological COMSOL models, with references included in the most-right column.

Material Properties	*Value(s), units and best-fitting trendlines*	*Reference(s)*
Density (Argon)	1.784 [kg/m³]	(Grigor & Steele, 1968)
Density (Rock)	2.300 [kg/m³]	(Laforce et al., 2022)
Dynamic Viscosity (Argon)	$2,22*10^{-5}$ [Pa/s]	(Grigor & Steele, 1968)
Permeability:		(Kuhlman et al., 2023b)
Undisturbed	10^{-21} [m²]	
Disturbed	10^{-19} [m²]	
Fracture	$3.8*10^{-14}$ [m²]	
Porosity:		(Kuhlman et al., 2023b)
Undisturbed	0,001 [1]	
Disturbed	0,01 [1]	
Fracture	0,1 [1]	
Specific Heat capacity	$-0,0045*T^2 + 3,9286*T + 0,722$ [J/kg*K] (from sample H-HP_2.5)	Experiments at WIPP
	$-0,0053*T^2+4,5976*T-143,33$ [J/kg*K] (from sample U-HP_6.4-6.25)	Experiments at WIPP
Thermal Conductivity	$-4,11\ln(T) + 28,142$ [W/m*K] (from sample H-HP_2.5)	Experiments at WIPP
	$-3,815\ln(T)+26,357$ [W/m*K] (from sample U-HP_6.4-6.25)	Experiments at WIPP

4. Model Results

4.1. Results of Step 0 Thermal Models

In Figure 6, three separate data sets are plotted: the experimental WIPP data (dotted lines), data set A (continuous line) and data set B (dashed line). The plot shows the temperature evolution over time for multiple sensors. Different line colors distinguish between sensors (F1 is blue, F2 is green, E2 is red, T2 is yellow, T1a is cyan and T1b is magenta). Data set A uses the thermal conductivity and specific heat capacity from the sample H-HP_2.5 and Data set B uses the parameter equations from sample U-HP_6.4-6.25.

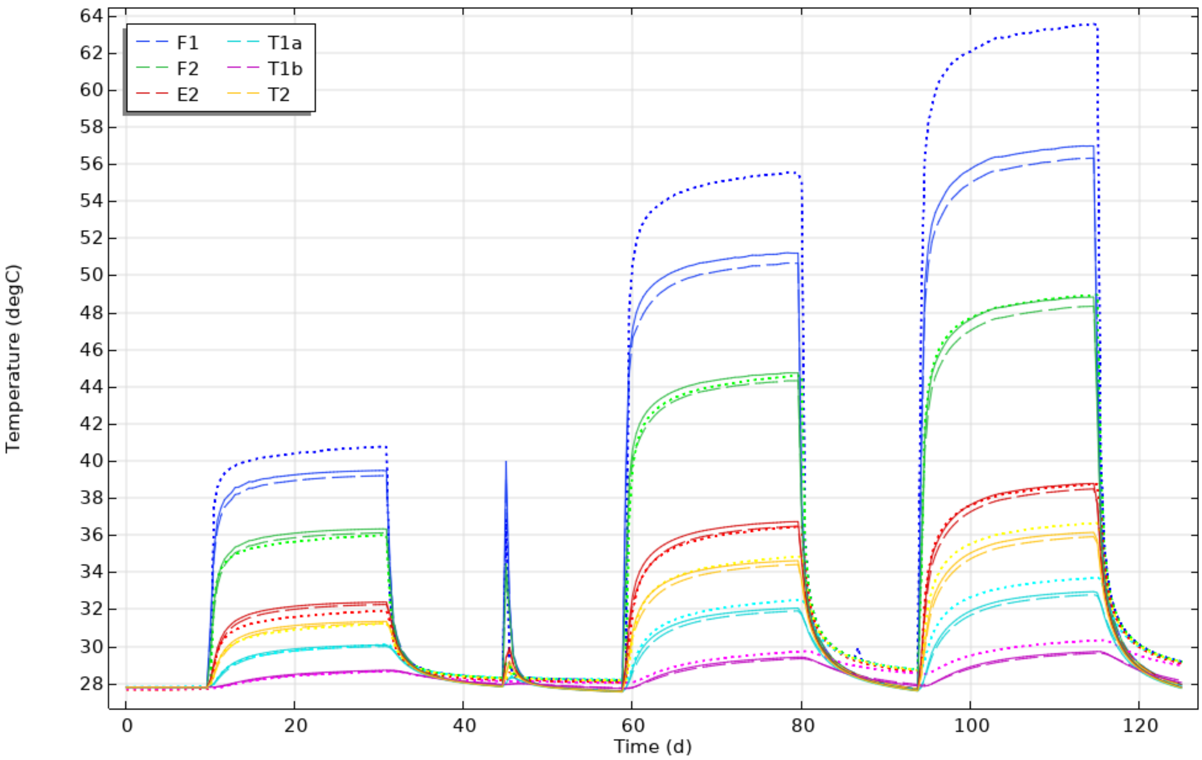

Figure 6: Temperature versus time plot. The continuous and dashed lines represent the COMSOL model data sets A and B respectively, while the dotted line is the experimental data from the WIPP site. The used material properties and COMSOL settings are described in the previous section. The sensors have the same color-coding as in Figure 3. The peaks at ~45 days are from an abandoned experiment; see text for explanation.

A good agreement between the experimental data and the model calculations was observed for all the sensors except the sensor F1. This sensor exhibited a distinct behavior compared to the other sensors, with the temperature discrepancy between the experimental results and the model predictions becoming progressively larger as the heater's radiated power increased. The three consecutive heating cycles have increasing power emitted, resulting in higher temperatures and increasing underprediction of the model results when compared to the experimental values, which can be seen by the increasing distance between the dotted line and the continuous line for data from sensors T1a, T1b and T2. The temperatures measured at F2 and E2 show increasingly better fits with higher temperatures, while these data sets show an overestimation at the earlier and cooler heating phases.

Every heating phase can be separated into three different phases: heating, quasi-steady-state (QSS) and cooling. The accuracy of the heating and cooling phases can be compared best by plotting the variation in temperature difference between the experimental data and the model results as a function of time (Fig.7). Sensor F1 is excluded from this graph, because the difference between the two data sets is much larger than for the other five sensors. Therefore, the F1 sensor temperature difference between the model calculations and WIPP experiment results is plotted in a separate graph (Fig. 8). The continuous line represents the model data from the data set A and the dashed line represents the data from set B. Both graphs display a clear dip at the start of the heating phase, followed by a peak after the heater is switched off. This pattern is consistently observed across all sensors. The initial dip suggests that the rock salt heats up faster than the model predicts. In contrast, the peak at the end of the heating phase indicates that in the COMSOL simulation, the rock salt retains heat longer and cools slower than measured. This discrepancy points to differences in thermal properties or heat transfer mechanisms between the experimental setup and the numerical model.

The QSS phase over every sensor in every heating phase can be evaluated with both graphs. The roughly horizontal lines in between the peaks at day 10 and day 30 as well as the period between the peak at day 60 and the valley at day 80 and the period between day 90 and 110 represent these steady-state period in which the fast heating of the rock salt body has stopped, and some minor heating is still on going. For sensor F2 and E2 higher temperatures result in a better fit, while the other three sensors (T1a, T1b and T2) show a greater misfit between experimental and model data with heater output.

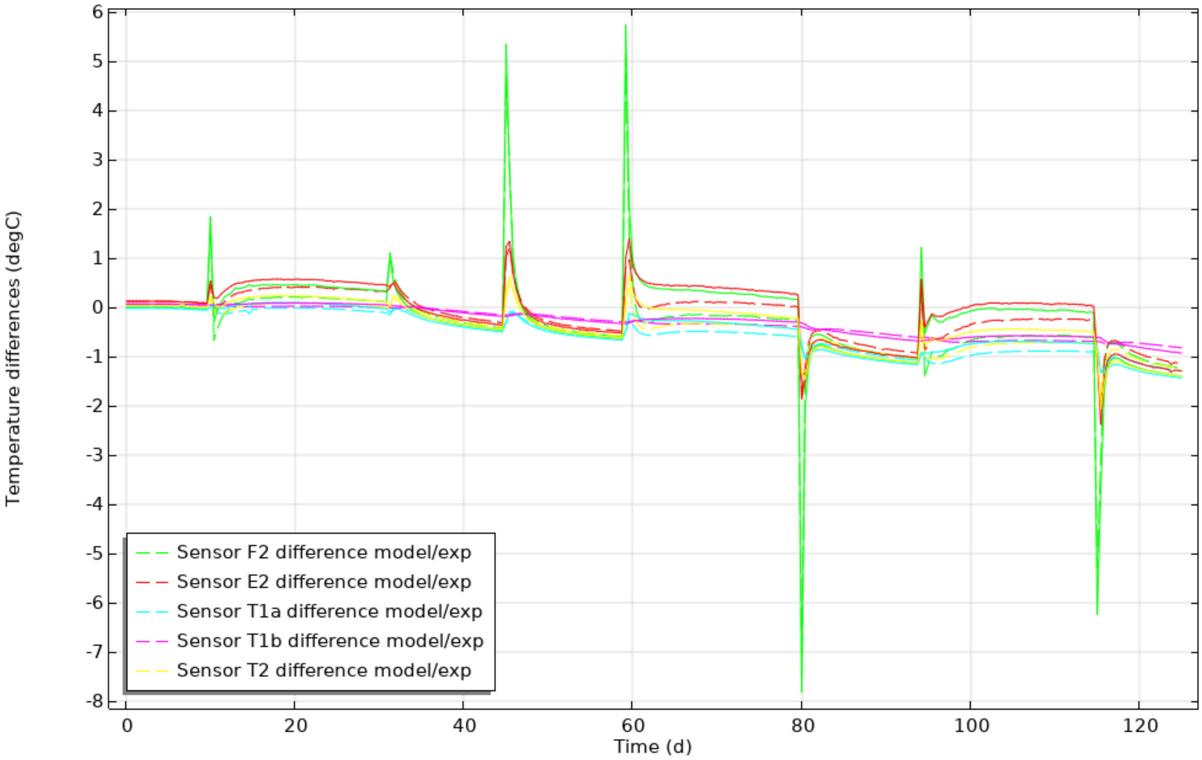

Figure 7: The difference between model predictions and experimental data. The F1 sensor is shown in a separate graph in Fig. 8, because of its considerably higher difference values.

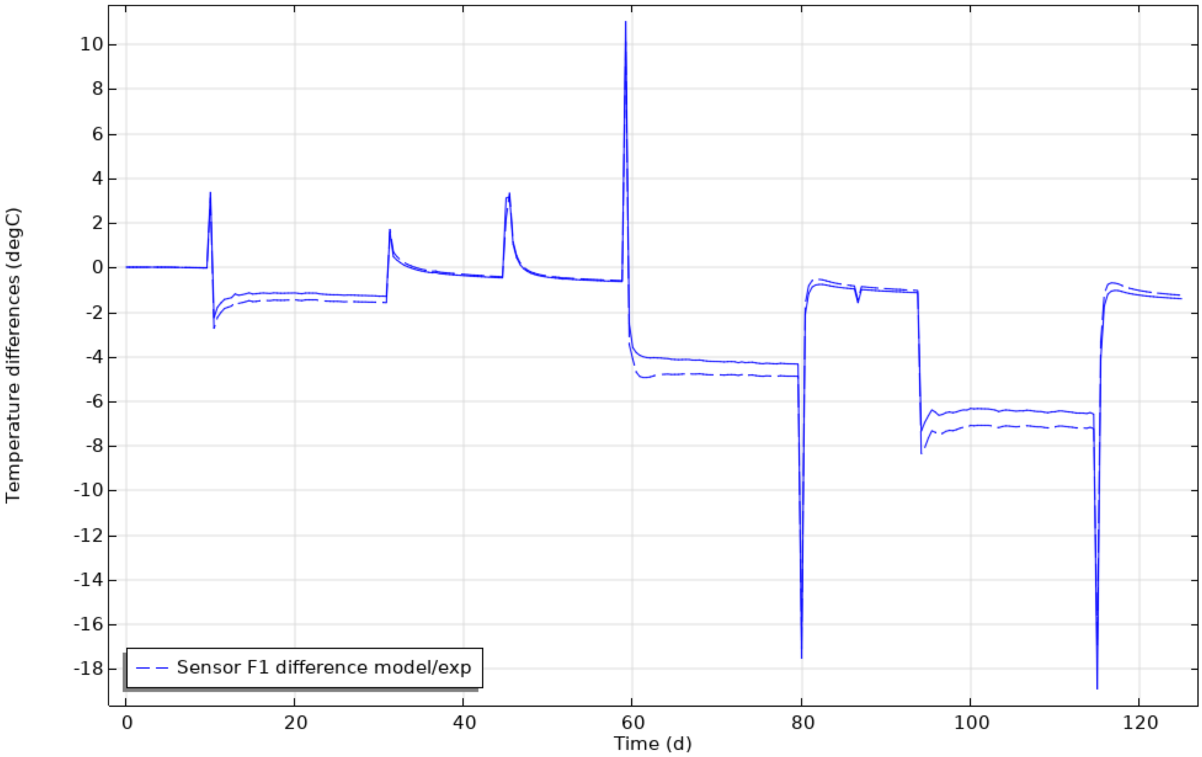

Figure 8: The difference between the calculated values and the outcome of the experiments of sensor F1, with the chosen material properties.

A notable feature of the graph is a short-lived temperature peak just after day 40. This anomaly resulted from an attempted heating phase that was abandoned due to a system malfunction. Despite its brief duration, this feature is visible in both data sets. Figure 9 focusses on this peak, and shows that the models data overestimates the temperature that was reached during the experiment at all sensors. There is also a small peak at day 89 in the measured data from sensor F1 (blue), which was caused by a fiber malfunction and quickly solved (Kuhlman et al., 2024).

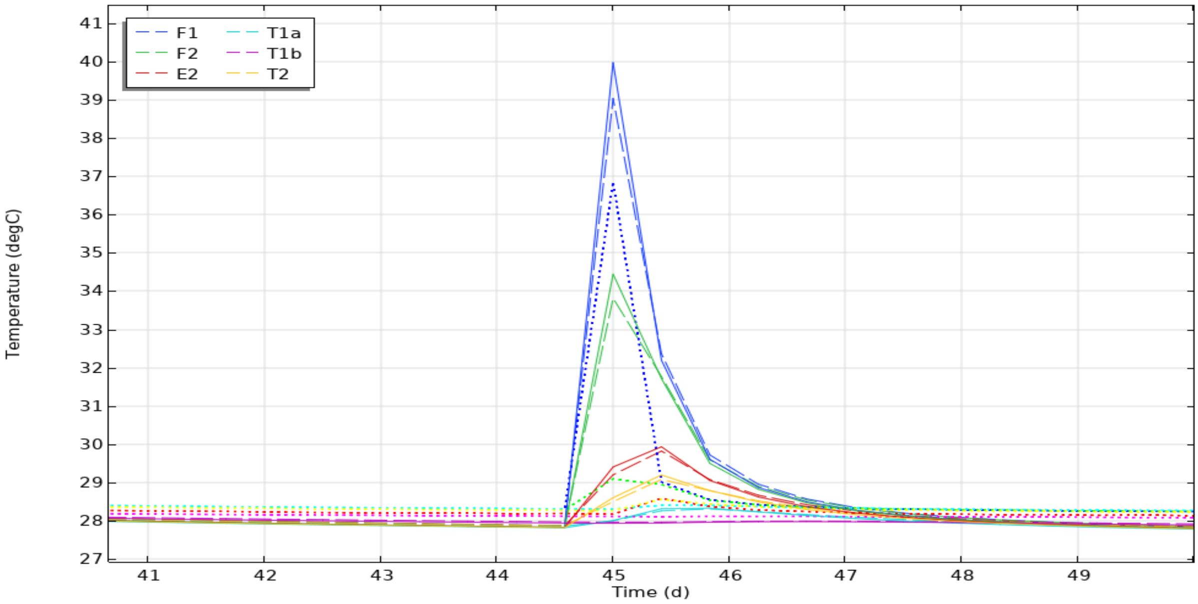

Figure 9: Temperature over time plot with the continuous and dashed line represent the COMSOL data and the dotted line is the experimental data from the WIPP site. This graph focusses on the small peak caused by the abandoned heating phase in between heating phase 1 and 2.

4.2. Parametric Studies of Step 0 Thermal Models

The temperature-dependency of the thermal conductivity and the specific heat capacity was obtained through experiments on rock samples from the WIPP. From the experimental thermal conductivity and specific heat capacity experimental data, multiple relations between the thermal conductivity/specific heat and temperature could be obtained. When focusing on the location of the samples, the H_HP_2.5 is closest to the heater, however the U-HP_6.4-6.25 (Figure 3) is originating from the same borehole. The other two sets of samples are from the SL borehole, located above the heater borehole. The locations of the boreholes are shown in Figure 3, in section 3.1.1. Geometry. Therefore, the specific heat capacity and the thermal conductivity from the sample U-HP_6.4-6.25 are also of interest. The equations of both parameters can be found in Table 1.

In Figure 5 both data sets are plotted with the dashed line representing the data set with parameters from sample U-HP_6.4-6.25. Comparison of the two different COMSOL data set results in minor differences between the two. The calculated temperatures for data set reveal a good agreement between the model predictions and the experimental results. However, when analyzing the temperature difference between the BATS II data and the COMSOL calculations over time, it becomes clear that the maximum deviation is larger when using parameters derived from rock samples originating from the HP borehole. This is particularly apparent when comparing the values along the x-axis of the graph (Fig. 5), which highlights the temporal progression of these differences. At the relatively low temperatures that are generated during the first heating phase, this data (with dashed line) shows a better fit than the data set represented by the continuous line. At higher temperatures, the difference between the values from this data set become larger than the values from the data set using the parameters from the H_HP_2.5 sample. This observation applies to every sensor.

4.3. Convergency Studies of Step 0 Thermal Models

To ensure the reliability and accuracy of the COMSOL model results, a convergence study was performed to examine the influence of mesh density on the quality of the model results. By systematically refining the mesh, we aim to evaluate the balance between computational efficiency and solution precision, identifying an optimal mesh configuration for the simulations. The results described in section 4.1 and presented in Fig.5 are obtained using a mesh with a total of 102365 elements. A coarser mesh with fewer elements (26250 elements) and a finer mesh with more elements (409456) were chosen to investigate the effects on the model calculations. For this convergency study (and the sensitivity study as well), only the first heating phase was simulated to make it easier to compare the data sets with each other.

Based on the results of the convergence study in Figure 10 and comparing the data sets from the dashed, continuous, and dashed-dotted lines, it was observed that increasing the number of mesh elements beyond a centimeter mesh scale did not result in significant changes to the calculated outcomes. Similarly, a coarser mesh with fewer elements produced results that remained consistent with those obtained using a finer mesh. This indicates that the solution has reached convergence.

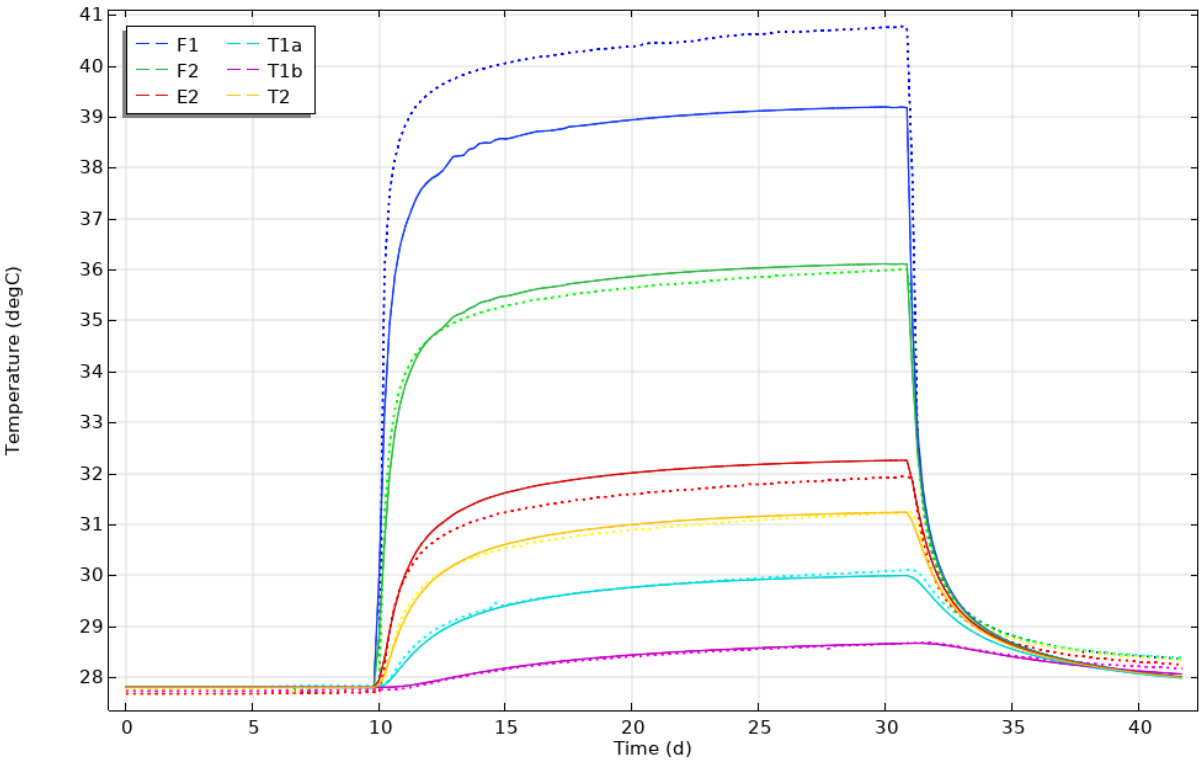

Figure 10: Temperature over time plot with the continuous line representing the mesh with102365 elements, the dashed line the coarser mesh (26250 elements) and the dash-dotted line representing the finer mesh (409456 elements). The dotted line is the experimental data from the WIPP site. The material properties from sample H_HP_2.5 were used, while the focus is on the first heating phase.

4.4. Sensitivity Analysis of Step 0 Thermal Models

To evaluate the robustness and reliability of the model, a sensitivity analysis was conducted to assess its response to variations in key input parameters. By systematically altering individual parameters (thermal conductivity and specific heat capacity) while keeping others constant, the analysis provides insight into the influence of each parameter on the model's outputs. To perform this analysis, an increase and decrease of two and five percent for both parameters was implemented. These two and five percentages were chosen to analyze the effect of small changes in both parameters.

Figure 11 displays the results of the two (dash-dotted) and five (dashed) percent increased values, together with the original (continuous) values and the experimental (dotted) data. The overall first-order shape and trends of the graphs are similar. However, the temperatures of the QSS part of the models with 2 and 5 percent increased parameters are consistently lower. This is due to the increased thermal conductivity and specific heat capacity, resulting in higher temperature gradients. The heating and cooling of the host rock occur at the same rate as during the experiments with the original values.

For analyzing the heating and cooling phases, the difference graphs as plotted in Figure 7, are also made for this new model setup. The greater the peak or valleys maximum value in this type of plot, the larger the discrepancy in warming or cooling between the model and the experimental data. Figure 12 shows the effect of a two percent increase for both thermal parameters to the three phases during the experiment. This effect is different for each thermocouple. The F2 sensor shows no noticeable difference in the cooling or heating of the host rock, whereas the E2 thermocouple shows a better fit: the dotted line is closer to zero during the heating and cooling phases as well as during the QSS phase.

The opposite effect can be observed when decreasing the values of both parameters by two and five percent (Figure 13). This results in increased QSS temperature values that will be reached at each sensor. Similar to the data obtained from increasing the values of thermal conductivity and specific heat capacity, the cooling and heating does not change from the experiments with the original values. Figure 14 shows the effect of a two percent decrease for both thermal parameters on the three phases during the experiment: this effect is different for each thermocouple. The E2 thermocouple showed a better fit with an increase, but does the opposite in this model setup, the dotted line is further away from zero during the heating and cooling phases as well as the QSS phase.

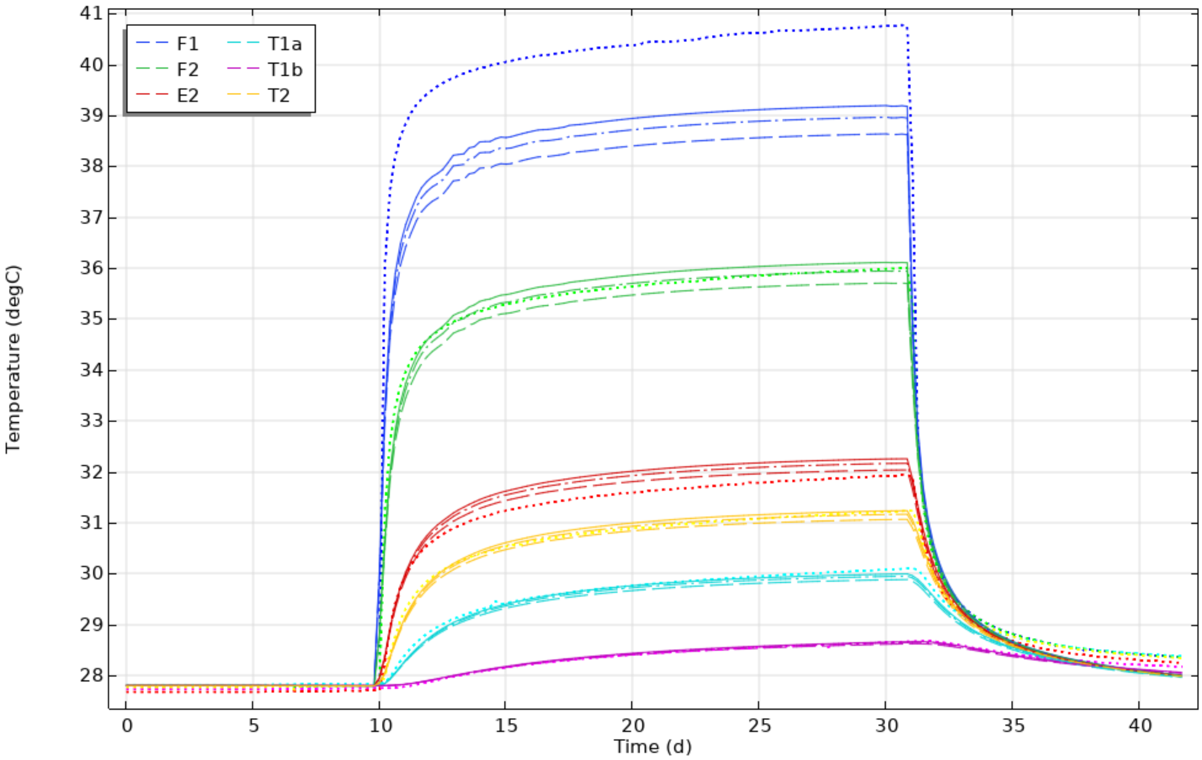

Figure 11: The data of two (dash-dotted) and five (dashed) percent increase were plotted together with the original (continuous) values and the experimental (dotted) data. The coloring of the sensors is the same as in earlier graphs in this report. Only the first heating phase is plotted for a more in-depth view of the changes in the system caused by the different values for the parameters.

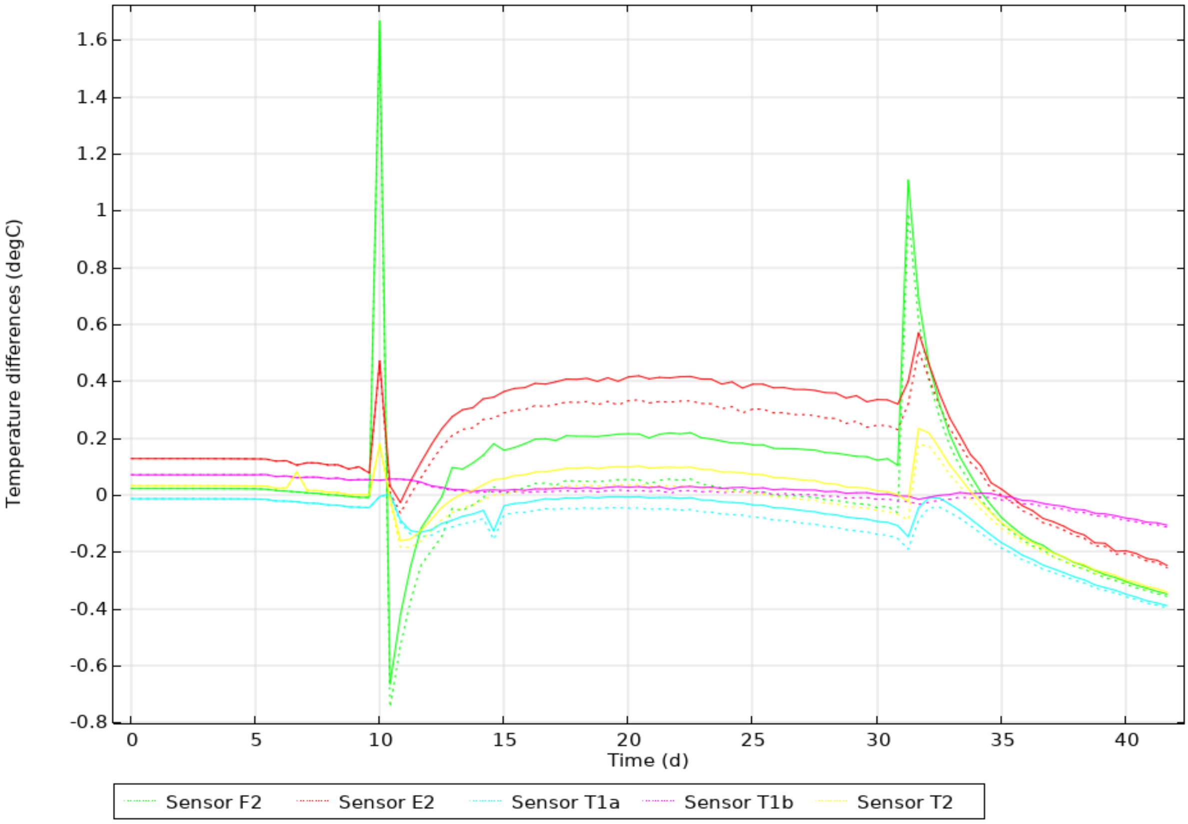

Figure 12: The difference between the model results and the outcome of the experiments, F1 sensor is excluded for readability purposes. The dotted lines are the new model setup with a two percent increase for thermal conductivity and specific heat capacity parameters, the continuous line is the original model setup plotted for easy comparison.

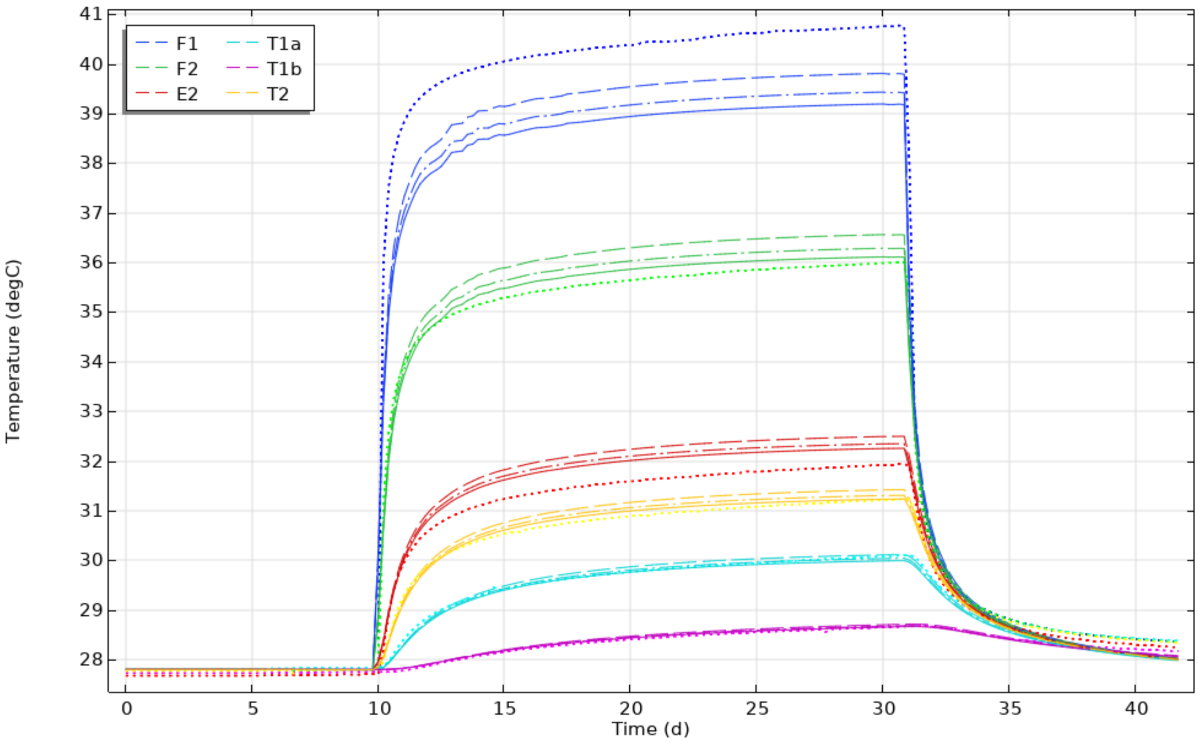

Figure 13: The data of the models with two (dash-dotted) and five (dashed) percent decreased thermal parameters were plotted together with the original (continuous) values and the experimental (dotted) data. The coloring of the sensors is the same as in earlier graphs in this report. Only the first heating phase is plotted for a more in-depth view of the changes in the system caused by the different values for the parameters.

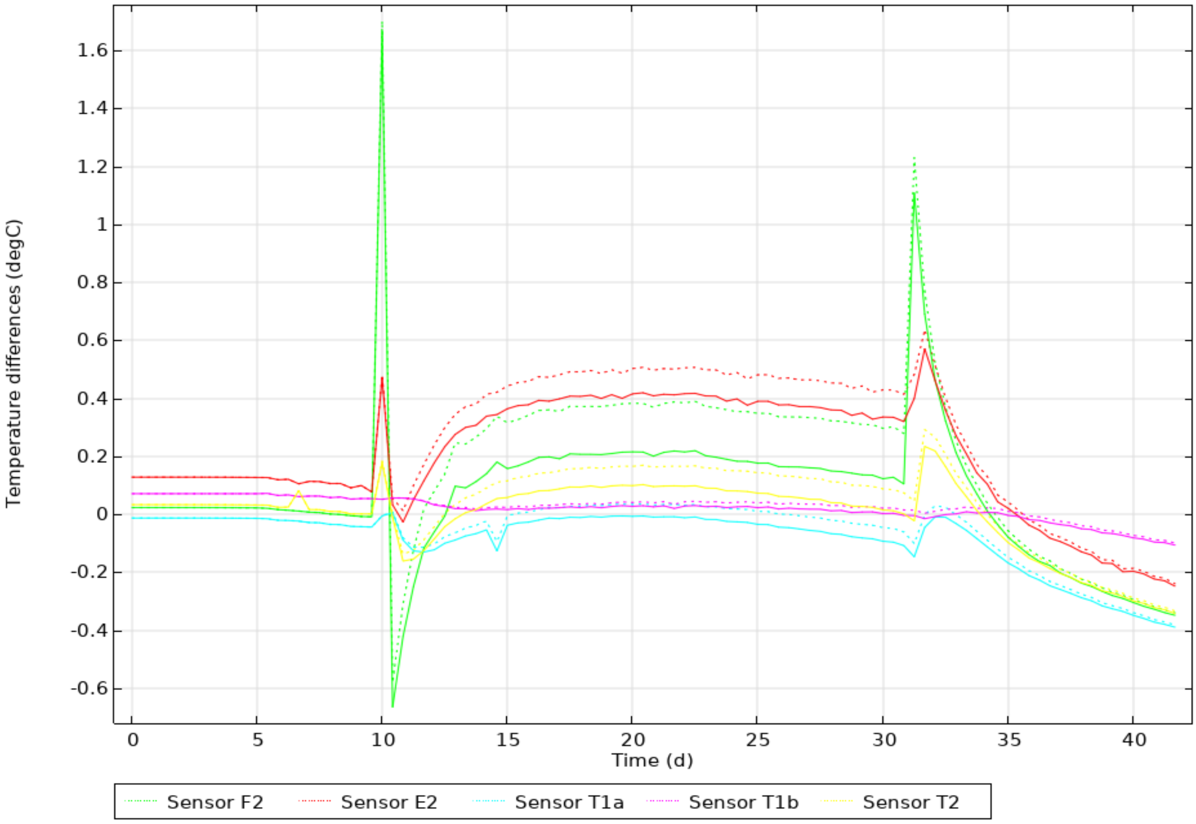

Figure 14: The difference between the model results and the outcome of the experiments, F1 sensor is excluded for readability purposes. The dotted lines are the new model setup with a two percent decrease for thermal conductivity and specific heat capacity parameters, the continuous line is the original model setup plotted for easy comparison.

The influence of each individual thermal parameter is also of interest. Figure 15 shows the model results with thermal conductivity raised by five percent and the specific heat capacity not changed, and Figure 17 displays the thermal conductivity unchanged while the specific heat capacity was raised by five percent.

These graphs show the influence of the specific heat capacity and the thermal conductivity, mainly on the steady-state temperatures. The overall shape of the graphs of the measured temperatures per sensor does not visibly change, only the temperatures that are reached at the steady-state changes noticeably. An increased thermal conductivity results in a significantly higher final temperature than a similarly increased specific heat capacity.

Figures 16 and 18 show the comparison between the two variations on the models setup by dividing the model results by the experimental results, resulting in a plot which indicates the relative difference between the two model outcomes. The change in specific heat (Figure 18) shows no significant difference between the two models. The change in the thermal conductivity results in a noticeable difference with the dotted and the continuous line. The dotted line is closer to a temperature difference of zero than the continuous line, meaning the modelled heating, cooling and QSS stages are closer to the experimental data.

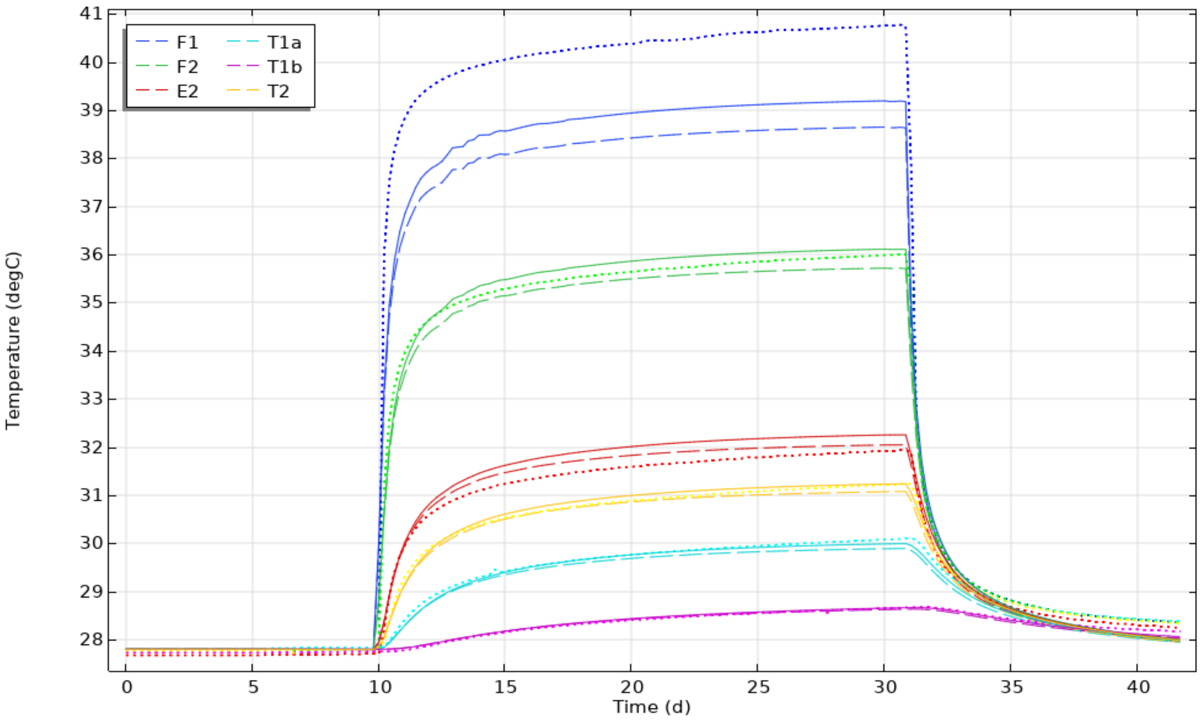

Figure 15: The data of five (dashed) percent increase of the thermal conductivity was plotted together with the original (continuous) values and the experimental (dotted) data. The coloring of the sensors is the same as in earlier graphs in this report. Only the first heating phase is plotted for a more in-depth view of the changes in the system caused by the different values for the parameters.

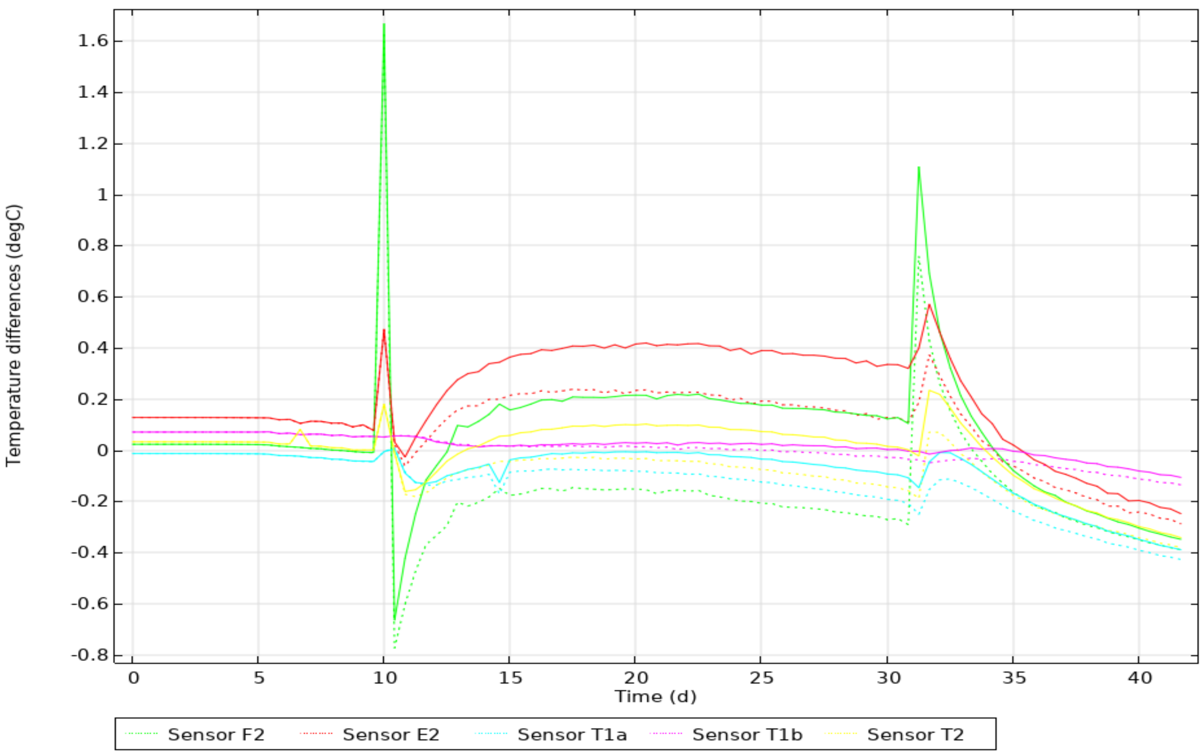

Figure 16: The difference between the model results and the outcome of the experiments. The F1 sensor is excluded for readability purposes. The dotted lines are the new model setup with a five percent increase for thermal conductivity, the continuous line is the original model setup plotted for easy comparison.

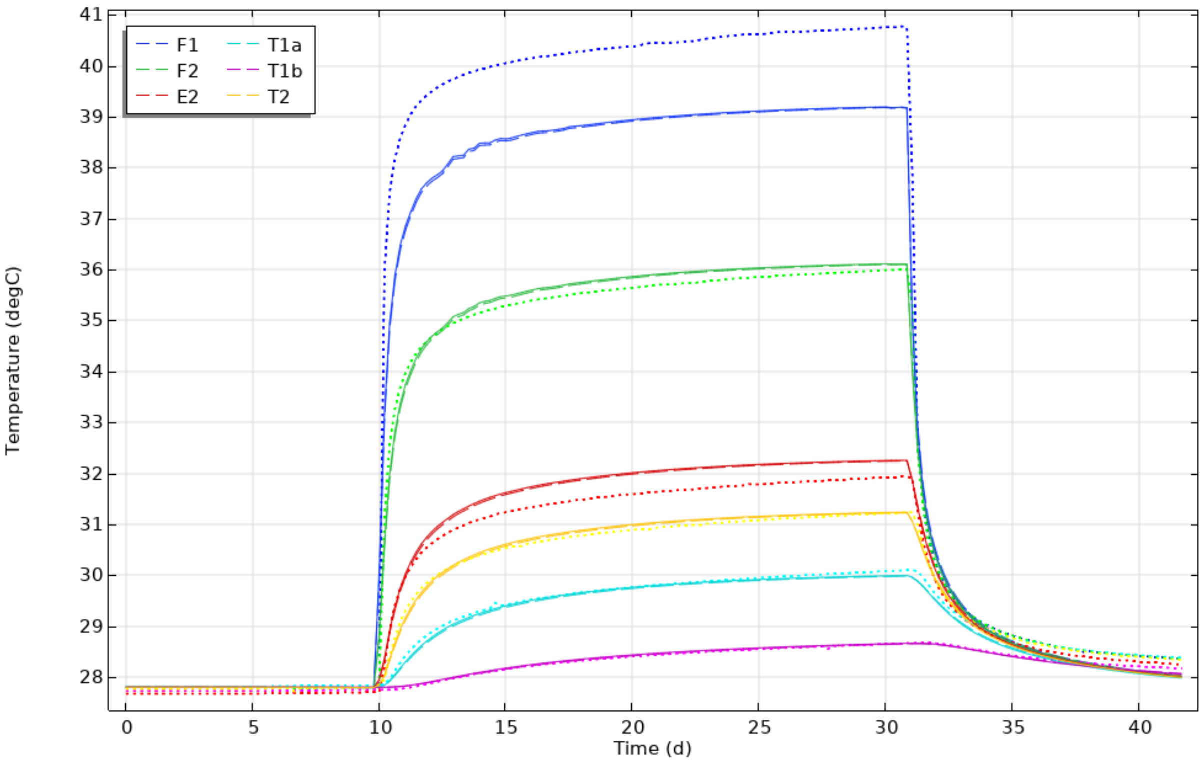

Figure 17: The data of five (dashed) percent increase of the specific heat capacity was plotted together with the original (continuous) values and the experimental (dotted) data. The coloring of the sensors is the same as in earlier graphs in this report. Only the first heating phase is plotted for a more in-depth view of the changes in the system caused by the different values for the parameters.

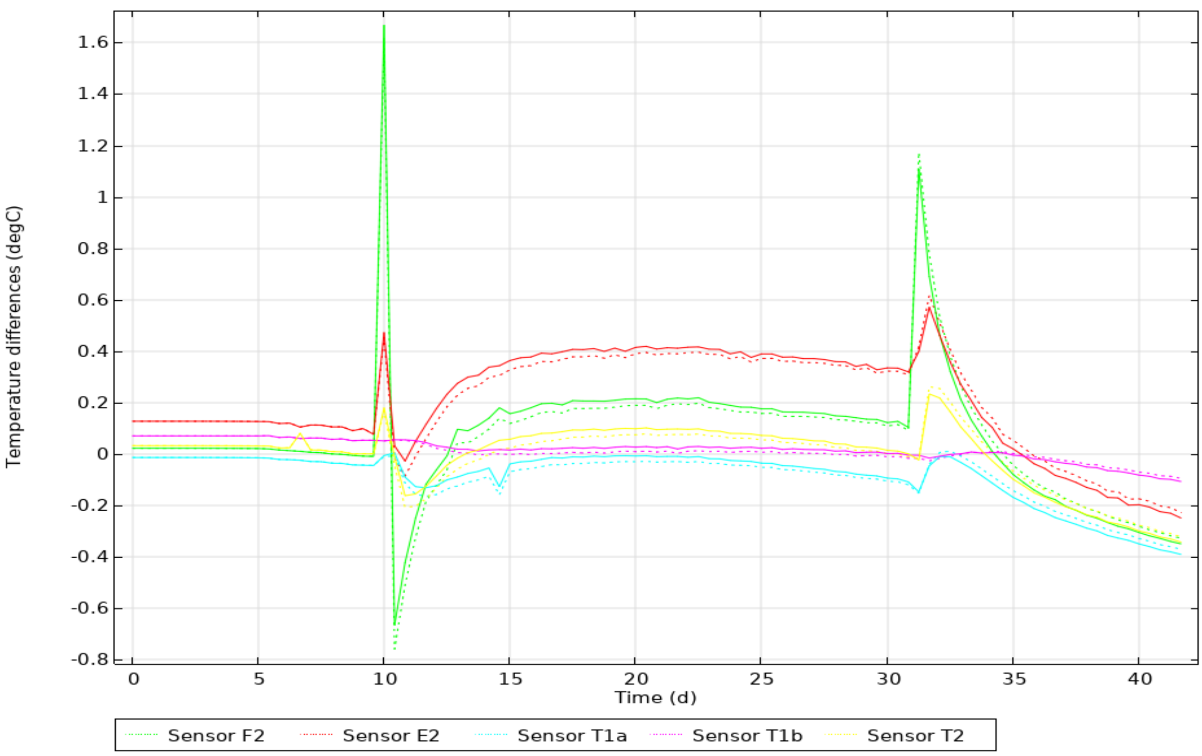

Figure 18: The difference between the model results and the outcome of the experiments The F1 sensor is excluded for readability purposes. The dotted lines are the new model setup with a five percent increased specific heat capacity; the continuous line is the original model setup plotted for easy comparison.

4.5. Results of Step 1 Thermal Model

Figure 19 illustrates the temperature evolution over time, comparing experimental results (dotted lines) with numerical simulations (solid lines) for different model datasets (F1, F2, E2, T1a, T1b, and T2). The x-axis represents time (days), while the y-axis shows temperature (°C). The difference with the first thermal experiment, is that this experiment consist of only one long heating phase, while the first thermal experiment consists of three smaller heating phases.

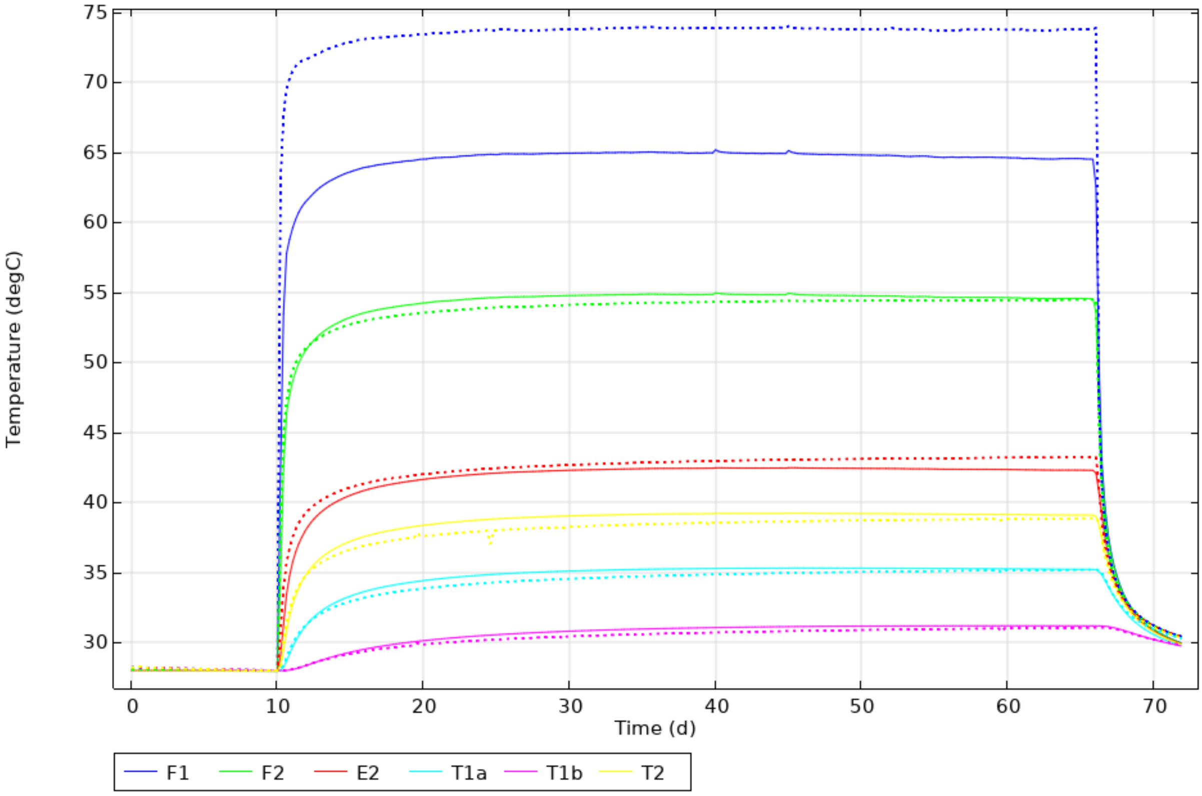

Figure 19: Temperature over time plot with the continuous line representing the COMSOL calculations and the dotted line is the experimental data from the WIPP site. The experiment consisted of one single heating phase, during which all sensors recorded the temperature.

The temperature profiles exhibit a sharp increase at approximately day 10, marking the onset of the heating phase, followed by a steady-state period before a rapid cooling phase at day 67. This heating phase corresponds to a controlled thermal input, with temperatures stabilizing at different levels depending on the sensor. The highest recorded temperatures are observed in dataset F1 (blue), peaking at approximately 72°C in the experimental data and 65°C in the model results, while other sensor location follow similar trends but with lower steady-state values. A direct comparison between experimental and simulated data shows that the numerical model generally underestimates the steady-state phase. Figure 16 showed that this misfit was largest, by 0.5°C on average, at the beginning of the heating phase and became less nearing the end of the heating phase. This underestimation is most pronounced in datasets with highest maximum temperatures (F1), see for instance Figure 17. Both experimental and simulated data capture this trend well, indicating that the heat dissipation behavior is reasonably well-represented in the model.

Figures 20 and 21 present a comparison between the experimental results and the model simulations. Both graphs exhibit a distinct valley at the beginning of the heating phase, followed by a peak after the heater is turned off, consistently observed across all sensors. The initial valley suggests that the rock salt heats up more rapidly in the experiment than predicted by the model. Conversely, the peak at the end of the heating phase indicates that the rock salt retains heat longer in the COMSOL simulation, cooling down more slowly than observed in the experiment. This discrepancy highlights potential differences in thermal properties or heat transfer mechanisms between the experimental setup and the numerical model.

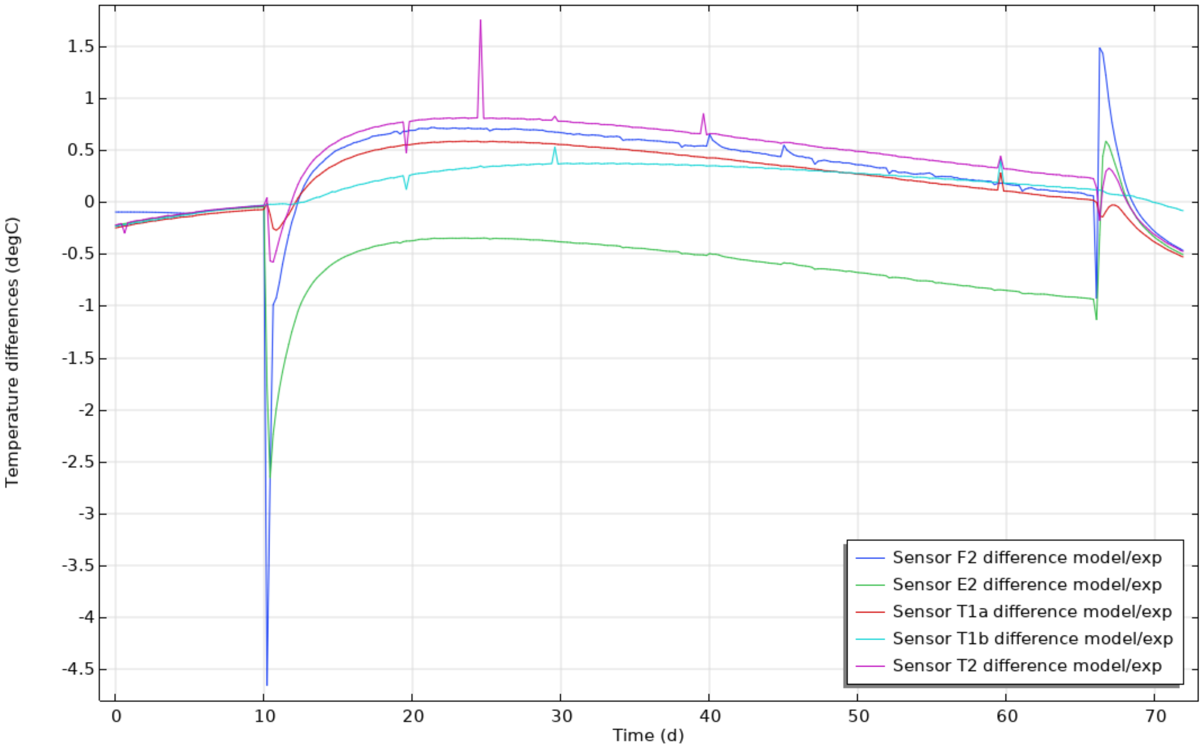

Figure 20: The difference between the results of the model and the experiments. The F1 sensor is excluded because the values are a lot higher than the other five sensors. The experiment consisted of one single heating phase.

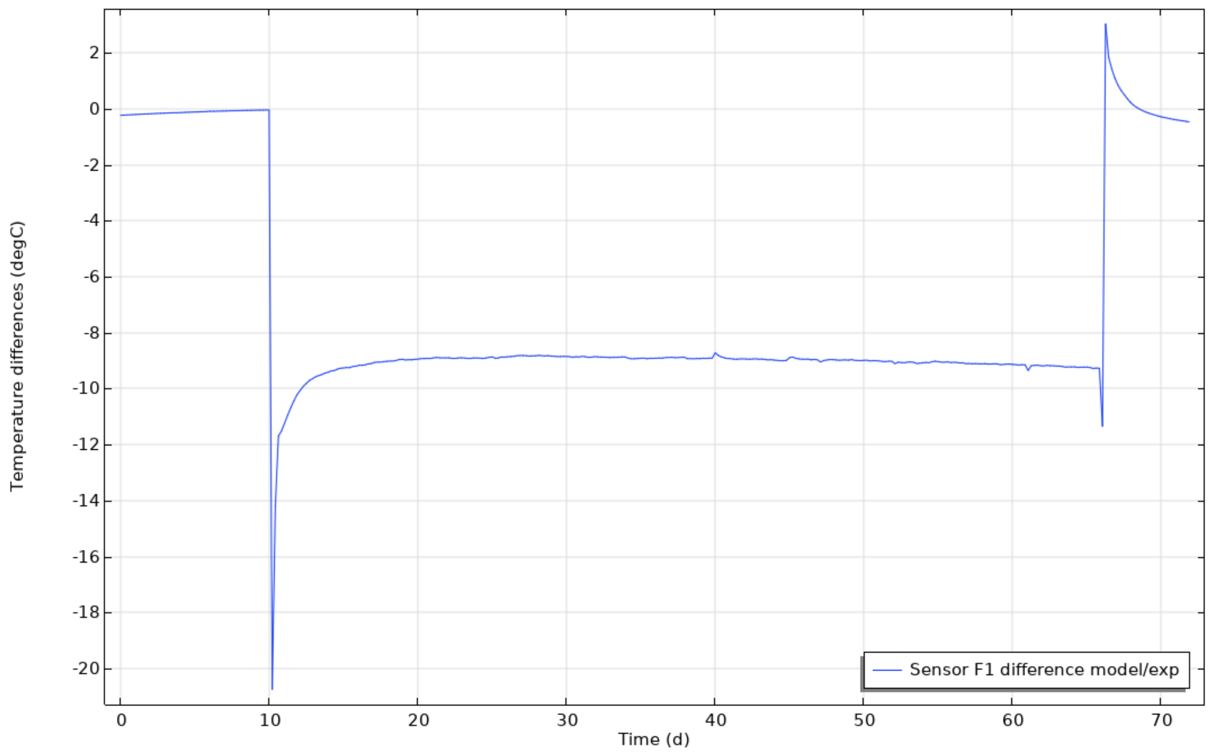

Figure 21: The difference between the results of the model and the experiments as recorded by the sensor in the F1 borehole. The experiment consisted of one single heating phase.

The small spikes that also appear in the comparison graphs (Figure 20 and Figure 21) are the result of measurement errors that were made during the runtime of the experiment in the WIPP.

4.6. Results of Step 1 Hydrological Model

Figure 22 presents the pressure evolution over time at the inlet, comparing model predictions (blue) with experimental data (green). The x-axis represents time, in days, while the y-axis shows pressure in psi.

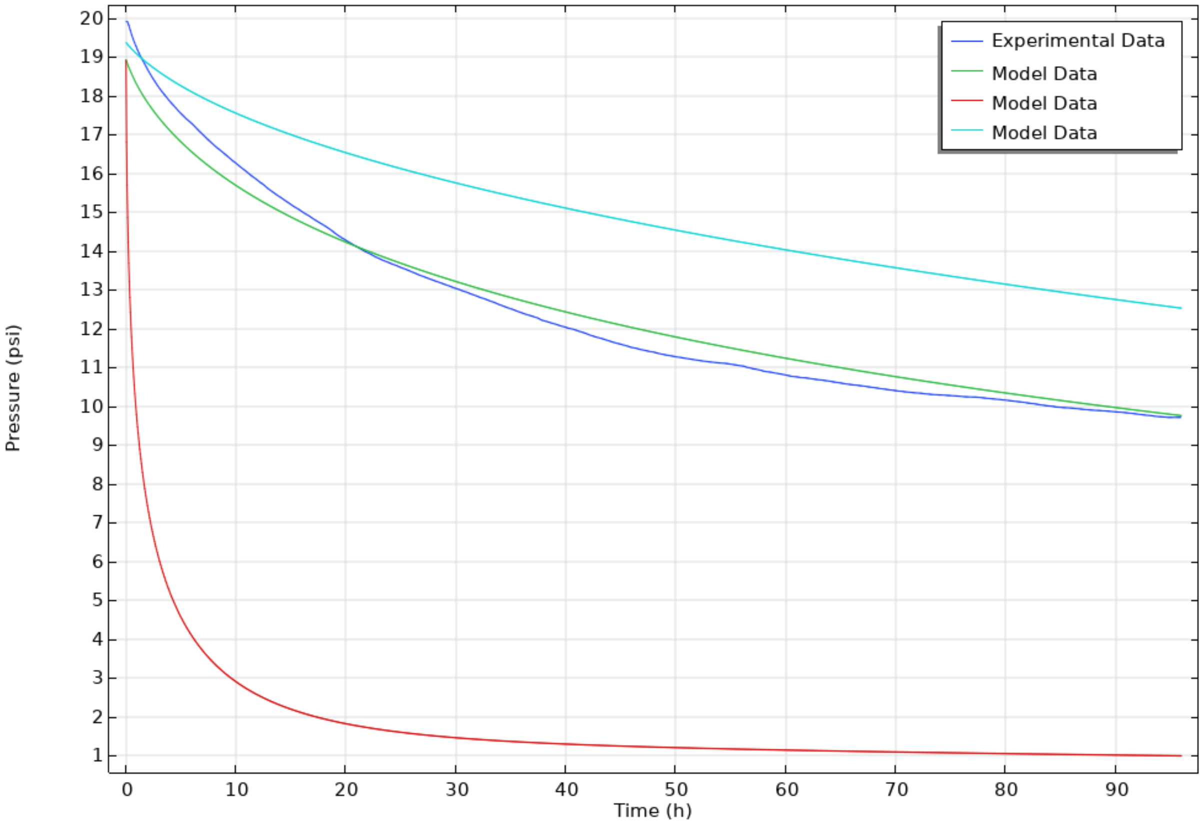

Figure 22: Pressure over time plot with the dark blue line representing the experimental results and the green line is the model results using the material properties as mentioned in the Model Setup section. The red and cyan line represents the model with other material properties as will be discussed in 4.7. The experiment ran for four days (96 hours), the pressure was taken from the surface of the inlet borehole.

Both the model results and the experimental data exhibit a general trend of decreasing pressure over time, indicative of a pressure dissipation process. The model and experimental data curves start at approximately 18.9 and 19.9 psi respectively, even though both had the same initial pressure values. At the start of the experiment both curves show a rapid initial drop in pressure. However, the model, at first, underestimates the pressure compared to the experimental data. The underestimation becomes an overestimation of the pressure value after 21.5 days.. This deviation becomes more pronounced as time progresses, with the largest difference occurring around the midpoint of the observation period (after 2 days). Towards the end of the observation period (around 3.5 days), the two datasets converge, indicating that the long-term pressure dissipation trend is captured reasonably well by the model. In summary, after a smaller drop at the onset of the experiment, the measured rate of pressure decrease is larger than the modelled rate during the first 2 days but smaller in the next 2 days, such that after 4 days the measured and modelled pressures at the inlet are (nearly) equal.

4.7. Parametric Studies of Step 1 Hydrological Model

Calculations with Darcy's law require several material parameters as input: porosity (Φ), permeability (k), fluid density (ρ_f), dynamic viscosity (μ). The two parameters that involve the gas behavior (ρ_f and μ) are well defined by literature and no variation is expected within the WIPP experimental site. In contrast, host rock properties can vary throughout the rock body, and heterogeneity is expected within the rock. Research reports from BATS I use permeabilities ranging from 10^{-19} to 10^{-21} and porosities that range from 0.01 to 0.001 (Kuhlman et al., 2023b). Changing the adopted values of these two parameters for the host rock body to the lower end of the parameter range yields model results that are represented in Fig. 22 by the red line. The value at the end of the experiment changes from 9.77 to 0.99 psi. This pressure drop is caused by more argon gas flowing from the borehole into the host rock instead of in the fracture, due to the increased pressure of the surround rock body. The modelled zone of increased permeability and porosity between the inlet and outlet, representing the proposed fracture, is defined using experimental data from the BATS II experiments. In Figure 22, the cyan line illustrates the pressure drop in the inlet over a four-day period when the fracture is removed from the model. The model's data does show significant change in pressure during the four days: the final pressure goes to 12.52 psi, which is 2.75 psi higher than the experimental measurements. A larger fraction stayed within the inlet borehole when compared to the model shown by the cyan line.

4.8. Convergency Studies of Step 1 Hydrological Model

To validate the reliability and accuracy of the hydrological model results, a convergence study was performed examining the influence of mesh density on the model results. Evaluation of the balance between computational efficiency and solution precision was done to identify an optimal mesh configuration for the simulations. This analysis not only demonstrates the sensitivity of the solution to mesh quality but also validates the chosen. The graph shown in Figure 22 is for a model with a total of 13554 elements. A coarser mesh with fewer elements (11252 elements), represented by the cyan line in Figure 23, and a finer mesh with more elements (17950), red line in Figure 23, were chosen to investigate the effects on the model calculations.

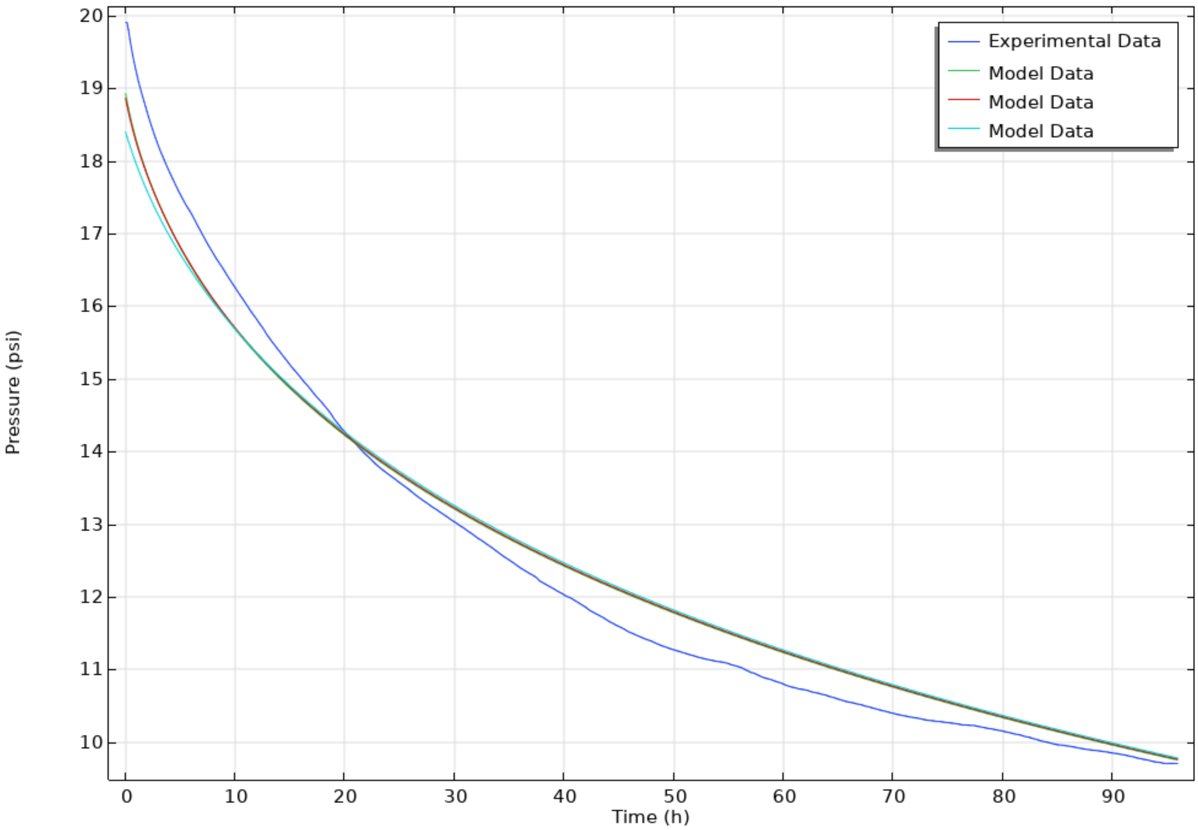

Figure 23: Pressure over time plot with the dark blue line representing the experimental results and the green line is the model results using the mesh with the number of elements mentioned in the Model Setup section. The red line represents a finer mesh (17950) while the cyan line represents the coarser mesh (11252 elements) model calculations. The experiment ran for four days (96 hours), the pressure was taken from the surface of the inlet borehole.

The convergence study and figure comparison show that increasing mesh elements beyond a centimeter threshold scale has a minor impact on results, and only in the first 10 hours. A coarser mesh yields different outcomes to a finer one. The final pressure differs the most from the experimental data when using the coarser mesh, and the difference between the experimental values and the model data differs slightly more with the finer mesh. However, the differences are very small and only noticeable at the rapid decrease of the pressure at the start of the experiment. This indicates convergence and ensuring reliable predictions without excessive computational time

4.9. Sensitivity Analysis of Step 1 Hydrological Model

In section 4.7, the influence of the material parameters was examined by changing the permeability and porosity of the host rock and fracture. The Darcy's Law Module in COMSOL uses the storage coefficient (S_P) for calculation. It represents the capacity of a material to store fluid under pressure and is used in hydrogeological and gas migration modeling. It accounts for both the compressibility of the fluid and the deformation of the porous medium.

The storage coefficient (S_P) has a distinct effect on the pressure drop over time in the model. Figure 24 shows the effect of decreasing the S_P value to $10^{-7.73}$ Pa/s with the red line and an increase to $10^{-5.73}$ with the cyan line.

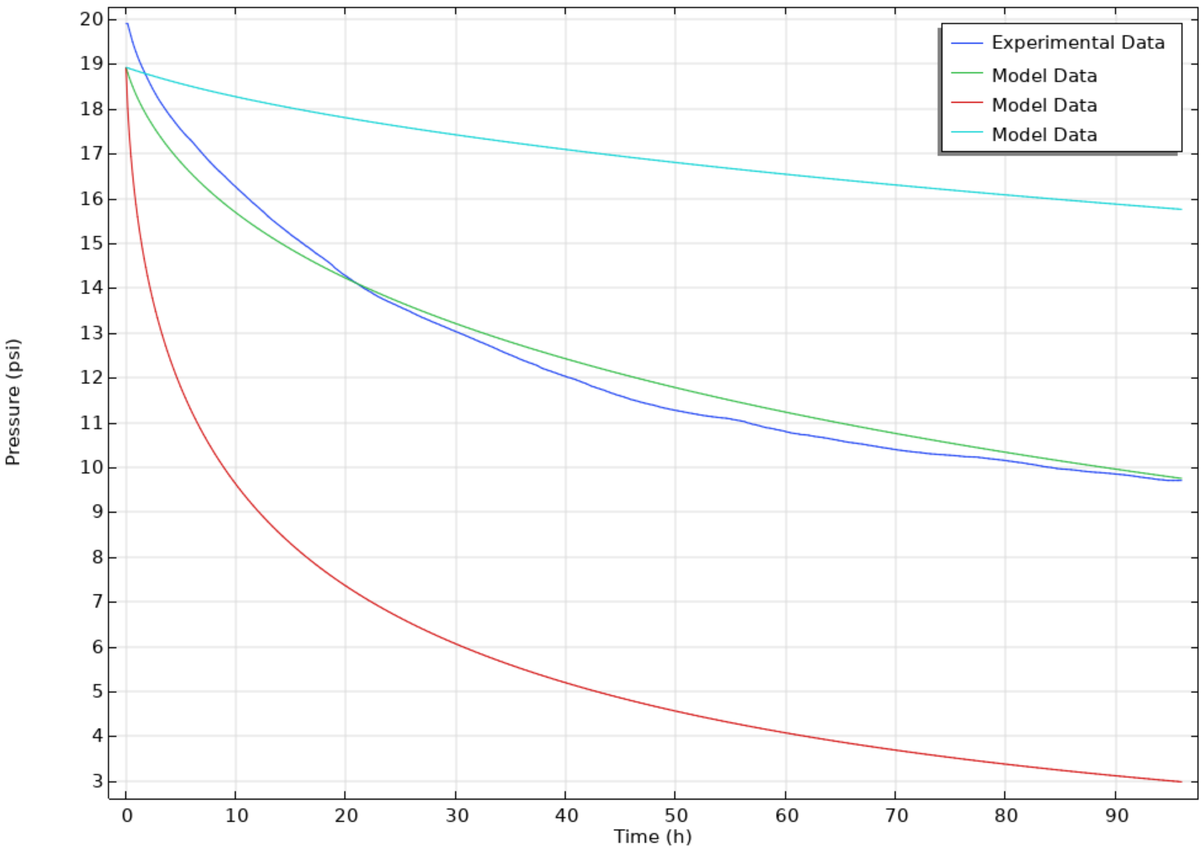

Figure 24: Pressure over time plot with the blue line representing the experimental data and the green line denote the values of the pressure with an S_P value of $10^{-6.73}$. The red line used a storage coefficient value of $10^{-7.73}$ and the cyan line uses a S_P value of $10^{-5.73}$.

Adjusting this parameter led to significant changes in the model results, altering both the shape of the pressure curve and the final pressure values compared to the experimental data. When the storage coefficient increased, the calculated pressure reached 15.76 psi, exceeding the experimental result. Conversely, reducing the storage coefficient caused a more rapid gas release into the surrounding rock salt. After four days the pressure settled at 2.99 psi. These findings highlight the sensitivity of the model to variations in the storage coefficient.

5. Discussion

The results of the two analyzed numerical thermal models with temperature-dependent specific heat capacity and thermal conductivity show that the heat transfer within the rock salt can be simulated satisfactorily. Within the axisymmetrical two-dimensional models, the rock properties are homogenous and isotropic, resulting in a radially symmetric heat conduction. The constructed models, in which the heater borehole is located in the center, correctly simulate the heat conduction in all directions.

The hydrological model, adopting material properties from the host rock and argon gas, correctly matches the pressure decrease over time before heating of the system starts.. Both the experimental and model data show a decay trend of pressure with time. The model data exhibits a smooth and exponential decay over time, with the rate of decrease slowing as time progresses. The experimental data also demonstrate an overall decreasing trend, however with a more rapid initial drop compared to the model data. The experimental curve also levels off more quickly, suggesting when compared to the model pressure curve an initially faster pressure decay rate followed by a slower decline.

5.1. Temperature-Dependent Specific Heat Capacity and Thermal Conductivity

The selected mathematical equations for the temperature-dependence of the specific heat capacity and thermal conductivity allow little variation as was visualized by the parametric (4.2.) as well as the sensitivity studies (4.4.). The DECOVALEX experiments on the temperature-dependence were also conducted on the grout that keeps the sensors in place within the boreholes. The outcome of this specific set of experiments showed that the specific heat capacity and thermal conductivity of grout is very different than for rock salt.

For thermal conductivity, the value was six to seven times smaller than the averages of rock salt at the temperature of 40 °C. Additionally the mathematic trend differs from that of rock salt with increasing temperature, a quadratic increase instead of a logarithmic decrease (see Appendix 6). For specific heat capacity, the value at 40 °C is 23% higher for grout than for rock salt samples from heater borehole and the mathematic trend with increasing temperature is again different between the two materials. With rock salt displaying a positive quadratic trend while grout showing a positive linear trend (See Appendix 5). Since this material is present in between the heater and the temperature sensors and has different properties, it is expected to change the outcome of the modelling, when included.

However, the thickness of the layer of grout between the heater and the sensor is decisive in how substantial the influence is on the critical parameters. The maximum thickness of grout between the heater and a sensor is 9.55 mm (Kuhlman et al., 2024). The F1 sensor is the thermocouple closest to the heater, at a distance of 19.30 cm. Therefore, 0.955 cm or 5% of the total distance would consist of grout. Adding the values of grout and rock salt together while taking their shares into account, the values for thermal conductivity will rise by 1.3% on average, whereas for the specific heat capacity the values will decrease by 2.0%. In short, a very limited change that will not lead to a substantial difference in the temperature calculations. For the other sensors located further away from the heater, this will be even less influential. In addition, in the two-dimensional axisymmetric COMSOL model all sensors are located along a line while in reality this is not the case. If every sensor was encapsulated by grout, the sensors furthest away from the heater (HT1TC10 and HT2TC10) will become too much influenced by the grout material properties, resulting in inaccurate simulations and temperature values. Hence, the grout material is not included in the COMSOL model

The experiments that resulted in the data for the step 0 thermal model simulations were conducted from July to November 2022. These experiments consisted of three different heating phases which were labelled as 2a, 2b and 2c. The experimental data for step 1 had been obtained from the beginning of June to the end of July 2024 and consisted of one heating phase which was labeled as 2g. In between these two experiments, a total of four heating phases were conducted (2d, 2e, 2f and one heating phases that was aborted after nearly one-and-a half day)(Kuhlman et al., 2025). These four heating phases were of variating duration and temperature. It is likely that the sequence of heating phases altered the abundance and size of fractures throughout the host rock and also changed the pore volume within the host rock.

Experiments on thermal conductivity and specific heat capacity, conducted to determine the temperature dependence of both parameters, utilized different samples from the WIPP experimental site. These samples were taken from the WIPP before the first heating phase was started, and were dried out before the thermal conductivity and specific heat capacity experiments were done. As mentioned above, the heating is likely to have altered the pore content in the rock salt body, which would have effectively simulated the drying of the samples that were used for the experiments at. Therefore, the thermal model used for the heating part of step 1 shows a better fit compared to the heating in step 0.

5.2. Homogeneity Versus Heterogeneity in the Thermal Models

The assumption that material properties are homogeneous throughout the rock body simplifies equations of the modeling process but may not fully capture the natural heterogeneity present in geological formations, especially in rock salt. Variations in mineralogy or pore content can alter properties such as thermal conductivity, specific heat capacity, and permeability. Ultimately this can significantly influence the accuracy of heat transfer simulations in real-world scenarios. Likewise, the heterogeneity at the start of the set of thermal experiments at the WIPP can also increase over time in a rock body due to the heating phases. During research by Roest and Gramberg (1984) on the thermomechanical cataclastic behavior of rock salt, acoustics were recorded immediately after the heating was turned off (Roest & Gramberg, 1984). These acoustic phenomena were also observed at the WIPP (Kuhlman et al., 2024) at the end of the heating phases. While the heater is on, the fractures in the rock close due to thermal expansion, reducing its porosity and permeability. Once the heater is turned off, the fractures reopen, causing additional damage due to the sudden pressure changes within the rock. Temperature variations in rock salt can lead to stress states in tensile regions, potentially generating discrete fractures (Staudtmeister et al., 2017). This can be observed in the rock through measurements of acoustic sounds that result from the cracking of pre-existing fractures that were previously closed due to thermal expansion. Consequently, after each heating phase, the damage to the rock may increase further (Staudtmeister et al., 2017).

The simulated graphs do not exhibit a consistent deviation from the BATS II experimental results. Instead, the graphs display peaks and valleys at the beginning and end of the heating phases, indicating that the heating and cooling processes in the COMSOL model occur either too quickly or too slowly. A peak after the heater turned on indicates that the model heats up too fast, while a peak during cooling down implies that the model cools down too slowly. Similarly, a measure trough is indicating that the model heats up too slowly or cools down too fast. This behavior in the graph is caused by the temperature-dependent equations for specific heat capacity and thermal conductivity. While the adopted values for both parameters seems to be correct at stable temperatures, the values differ from nature during transient phases of increasing and decreasing temperature. The used formulas can therefore be refined to better fit these periods.

Calculations on heating and cooling of rock bodies is a combination of specific heat capacity, thermal conductivity and density of the rock of interest. Changing the ratio between these three parameters results in different heating and cooling rates within the rock (Robertson, 1988). In the sensitivity study, the ratio between the thermal conductivity and specific heat capacity was changed, with density kept constant throughout all the data sets. However, the predicted rate at which the rock heated up and cooled down during the experiment did not change in the models, possibility because the size of the ratio change was not significant enough in the investigated models.

5.3. Sensor F1's Deviation Between Experiment and Model

All sensors except the sensor closest to the heater, HF1TC2, show a good fit between the experimental and model data. Using the homogenous material properties, the model predicts the temperature to be significantly lower than the temperature measured by the deviating F1 sensor during the experiments. The location of the F1 sensor is important to take into consideration. Looking from the drift face to the locations of the boreholes, the F1 sensor is located below the heater. The F2, T1 and T2 sensor are located on the left of the heater and the E2 sensor is located on the right and below the heater (Figure 3). No other sensor is in line with the heater and sensor F1.

The two critical parameters that affect the model results are the thermal conductivity and the specific heat capacity. The sensitivity analysis showed that decreasing the specific heat capacity and thermal conductivity values will result in higher temperature measured at the sensors. However, this study also showed that raising the specific heat capacity while lowering the thermal conductivity will also raise the temperature measured at the sensors. Within the host rock salt, water and air can also be present in pores and fractures. Both brine, with a specific heat of 3500 J/kg*K and a thermal conductivity of 0.55 W/m*K (Dittman, 1977), and air, with a specific heat capacity of 1005 J/kg*K and a thermal conductivity of 0.025 W/m*K (Gopal, 2012), have significant different values for both parameters. Presence of air and/or brine in a fracture between the F1 sensor and the heater is a possible explanation of the difference between the calculated and the measured temperature.

Another possible explanation for the difference between the model results and the experimental measurements can be found in the reference work (Kuhlman et al., 2024). In between the experiments at the WIPP, a temperature increase was measured at sensor F1 and F2 even after the heater was turned off. It was hypothesized that the sensor cables are not free of strains due to the large deformation of the rock salt around the cables. It was suggested that the bending pushed the temperature cable away from the heater (Kuhlman et al., 2024).

It should be noted that both explanations for the difference between the model results and the experimental data can be in effect simultaneously.

5.4. Single-Phase Flow in the Hydrological Model

Within COMSOL Multiphysics the Darcy's Law Module was used for the hydrological simulations. One of the major assumptions made when calculating with Darcy's law is to assume single-phase flow. Single-phase flow refers to the movement of a single fluid phase (liquid or gas) through a porous medium, such as rock or soil. In this type of flow, only one state of matter is present, simplifying the physical interactions involved. Key properties governing single-phase flow include the fluid's viscosity, density, and pressure gradient, as well as the permeability of the medium it flows through (Dullien, 1975). However, the rock salt at the WIPP has brine as the main component of the pore content. So, when introducing argon gas to the system, at least two phases would be present in the rock and interact with each other. Therefore, Darcy's law calculations may not be suitable. However, the heating and cooling cycles generated by the heater and causing thermal expansion and contraction influence the pore content. As the rock expands, the pore volume decreases, leading to an increase in internal pore pressure. This elevated pressure forces the brine out of the pores, pushing it away from the heated rock salt. The farther the brine is from the heat source, the less the internal pore pressure rises during the heating phase. After multiple heating phases, most of the brine is assumed to have been expelled from the experimental site, and only a small amount of brine is expected as leftover. Therefore, validating the assumption that one-phase flow was present and Darcy's law was made.

The initial pressure of each hydrological model is displayed differently in the graphs than the true initial pressure of (20.3 psi). This results in a seemingly underestimation of the pressure at the start of the simulation, and later on turns into an overestimation (in most situations). This incorrect display of the initial pressure is caused by the time stepping algorithm in the COMSOL software. This model starts with the first calculation at 0.2 hours after the experiment has started, this ensures that some of the gas has already migrated into the fracture and host rock, reducing the pressure in the inlet borehole.

5.5. Storage Coefficient Dependency

The sensitivity analysis of the hydrological model showed the influence of the storage coefficient on the model's behavior. Unlike directly measurable properties such as porosity or permeability, the storage coefficient represents both the compressibility of the fluid and the deformability of the solid matrix, making it a derived rather than intrinsic material property. A higher storage coefficient means more fluid can be stored per unit pressure change, leading to slower pressure dissipation. Conversely, a lower value results in more rapid fluid release and pressure equilibration. A proper calibration of the storage coefficient is essential for accurately simulating pressure changes and fluid flow in porous materials like rock salt.

The storage coefficient of rock salt is influenced by factors such as the compressibility of the rock matrix and the fluid in the pores and fractures combined with the porosity and permeability. Rock salt, with its low permeability, porosity and compressibility, has a low storage coefficient, as expected. However, no measurements, if any, done on rock samples originating from the WIPP have been published. Values for the storage coefficient in other rock formation range from 10^{-8} Pa^{-1} to 10^{-11} Pa^{-1} (Mctigue, 1993). Precise measurements for specific storage in rock salt are scarce in the literature. Given the unique properties of rock salt, such as its tendency to deform plastically and self-seal fractures, the specific storage is expected to be lower than that of more permeable and elastic-brittle rock types.

The lack of understanding of the storage coefficient is highlighted by Mctigue (1983) in his research on rock salt as possible suitor for radioactive waste depository host rock. His estimations range from 10^{-8} Pa^{-1} to 10^{-11} Pa^{-1} with the footnote that local heterogeneity can result in significant difference throughout the rock body (Mctigue, 1993). Permeability and porosity influence the storage coefficient together with pre-existing fractures. Moreover, the burial depth of the formation (lithostatic pressure), the presence of brine and grain size are other key characteristics that influence the value of the storage coefficient at a certain location (Mctigue, 1993). Other research by RIVM among others focused on modeling small-scale brine-inflow experiments (Beauheim et al., 1997). With the use of permeability values ranging from 10^{-20} m^2 to 10^{-21} m^2 and porosity values 0.001 to 0.03, the value for the matrix compressibility was calculated at $2.69*10^{-11}$ Pa^{-1}. For rock salt, the storage coefficient is mainly controlled by the matrix compressibility and formations thickness. With the use of the values presented by the RIVM in (Beauheim et al., 1997), the value of storage coefficient can be estimated ranging from 10^{-7} - 10^{-8} Pa^{-1}. This is closer to the value used for this study than Mctigue used for his research. For the model data in Beauheim et al. (1997), experimental data on permeability and porosity from rock samples from the WIPP were used, this data came from (Beauheim et al., 1991) were used. The difference with the values from Mctigue (1993), which also used rock samples from the WIPP, is significant and illustrates the heterogeneity of this parameter throughout a rock formation.

5.6. Influence of Temperature Increase on Gas Migration

The second research question of BATS II consists of two distinct aspects, thermal and hydrological, which are ultimately integrated. Step 1 aims to model the pressure decrease due to gas migration between boreholes under both ambient and heated conditions. This aim is similar to the objective of the BATS II project, which is to simulate the observed thermal-hydrogeological-mechanical (THM) responses recorded during experiments in the bedded salt at WIPP. Step 1 links these three components: the thermal aspect is driven by temperature increases from the heater, the hydrogeological aspect involves gas migration, and the mechanical aspect accounts for the thermal expansion behavior of rock salt in heated conditions.

Continuation of step 1 will focus on linking the thermal data to the permeability and porosity in the host rock, to better simulate the effects of thermal expansion. Reduced permeability, porosity and closure of fractures will change the possibility of gas migration within the experimental setup at the WIPP. It is expected that the temperature increase will cause thermal expansion, which can be implemented by COMSOL. A possible approach to incorporating this into the hydrological model, and ultimately integrating it with the thermal model, is by implementing a temperature-dependent internal pressure, where internal pressure increases with rising temperature.

5.7. Uncertainty in the Computational Models

Modeling uncertainties stem from assumptions, parameter estimations, and computational limitations. Evaluating these uncertainties is essential to ensure the reliability, validity and interpretability of the results. The experimental data does also have imprecisions caused by the measurement equipment. The COMSOL model uses experimental data as well as mathematical temperature dependencies of the specific heat capacity and the thermal conductivity. The uncertainties from the COMSOL model continue from the input data of the experiment, the thermal conductivity and specific heat capacity equations.

The thermocouples that are used to measure record the temperature during the experiment. This type of equipment had an absolute measurement uncertainty of 1 - 2 °C, while they are more accurate for capturing changes with time with an uncertainty of 0.1 - 0.2 °C. The heater output value and the thermocouples are the components from the experiments that give rise to an uncertainty.

Conclusion

The numerical modeling performed in COMSOL Multiphysics provided insights into the temperature-dependency of specific heat capacity and thermal conductivity connected to heat conduction in rock salt as well as the migration of gas through the rock salt at the WIPP. The results show that thermal conductivity and specific heat capacity are important factors in governing heat distribution within rock salt, directly influencing temperature gradients. Both parameters are temperature dependent: for the specific heat capacity the formula $-0{,}0045*T^2 + 3{,}9286*T + 0{,}722$ [J/kg*K] is used, and for the thermal conductivity the equation $4{,}11\ln(T) + 28{,}142$ [W/m*K]. The mathematical formulations of these parameters are highly specific to the rock samples, with even minor variations leading to shifts in the steady-state temperatures recorded by each sensor. Additionally, the heating and cooling processes in the computational model occur at a faster rate compared to the observed behavior at the WIPP experimental site. This might be due to limitations and simplifications of the models. The assumption of homogenous permeability, thermal conductivity and specific heat capacity, for example, may introduce uncertainties or influence the model results. Therewithal, the model was simplified with the omission of grout surrounding the thermocouple. These assumptions and simplifications were applied to maintain the model's feasibility and avoid unnecessary complexity.

The results of this study contribute to the (quantitative) evaluation of rock salt as a potential host rock for radioactive waste disposal by improving predictive models for long-term repository performance, specifically the heat generating period. The findings emphasize the importance of incorporating coupled thermal-hydrological-mechanical (THM) interactions in safety assessments to ensure more accurate predictions. Future research will aim to refine the modeling of mechanical deformation, integrate experimental validation, and extend the approach to include long-term creep behavior and stress-induced permeability changes.

Acknowledgments

I wish to thank the following people, without whom I would not have been able to complete this research. My Covra supervisor Dr. Jeroen Bartol is thanked for giving me the opportunity and guidance to conduct this research and sharing their knowledge and insights. My UU supervisor dr Fred Beekman is also gratefully acknowledged for insightful discussions over the course of this internship and for his guidance. I would also like to thank the people that reviewed this report, whose comments helped to improve this paper.

References

Beauheim, R., Ait-Chalal, A., Vouille, G., Tijani, S., McTigue, D., Brun-Yaba, C., Majid Hassanizadeh, S., van der Gissen, G., Holtman, H., & Mollema, P. (1997). *INTRAVAL Phase 2 WIPP 1 Test Case Report: Modeling of Brine Flow Through Halite at the Waste Isolation Pilot Plant Site*.

Beauheim, R. L., Saulnier, G. J., & Avis, J. D. (1991). *Interpretation of Brine-Permeability Tests of the Salado Formation at the Waste Isolation Pilot Plant Site: First Interim Report*.

Berkers, E., Lagendijk, V., Dekker, R., Snijders, D., & van Est, R. (2024). *Een kwestie van tijd Besluitvorming over radioactief afval in Nederland van 1945 tot 2016*.

Birkholzer, J. T., Tsang, C. F., Bond, A. E., Hudson, J. A., Jing, L., & Stephansson, O. (2019). 25 years of DECOVALEX - Scientific advances and lessons learned from an international research collaboration in coupled subsurface processes. In *International Journal of Rock Mechanics and Mining Sciences* (Vol. 122). Elsevier Ltd. https://doi.org/10.1016/j.ijrmms.2019.03.015

Bodansky, D. (2007). *Nuclear energy, principles, practices, and prospects: Second edition*.

Borns, D. J., & Stormont, J. C. (n.d.). *SANDIA REPORT An Interim Report on Excavation Effect Studies at the Waste Isolation Pilot Plant: The Delineation of the Disturbed Rock Zone*.

Callister, W. D. ., & Rethwisch, D. G. . (2021). *Materials science and engineering : an introduction*. John Wiley and Sons Australia, Ltd.

COVRA, N. V. (2024). *Masterplan 2050*. www.covra.nl

Dullien, F. A. L. (1975). Single Phase Flow Through Porous Media and Pore Structure. In *The Chemical Engineering Journal* (Vol. 10). Elsevier Sequoia S.A.

Dutch Government. (2024). *Step by step, the Netherlands is transitioning to sustainable energy*. https://www.government.nl/topics/renewable-energy/step-by-step-the-netherlands-is-transitioning-to-sustainable-energy

Energy Agency, I. (2025). *World Energy Outlook 2024*. www.iea.org/terms

Gao, W., Ullah, S., Zafar, S. M., & Usman, A. (2024). How does nuclear energy consumption contribute to or hinder green growth in major nuclear energy-consuming countries? *Progress in Nuclear Energy*, *170*. https://doi.org/10.1016/j.pnucene.2024.105111

Grigor, A. F., & Steele, W. A. (1968). Critical properties of argon. *Physics and Chemistry of Liquids*, *1*(2), 129–139.

Gutting, A., Högselius, P., Meyer, T., & Mbah, M. (2024). *Geographies of Nuclear Energy. An Introduction*. https://doi.org/10.2307/27290652

Kuhlman, K. L., Bartol, J., Benbow, S., Bourret, M., Czaikowski, O., Guiltinan, E., Jantschik, K., Jayne, R., Norris, S., Rutqvist, J., Shao, H., Stauffer, P., Tounsi, H., & Watson, C. (2023b). *DECOVALEX-2023 Task E Final Report*.

Kuhlman, K., Mills, M., Jayne, R., Matteo, E., Herrick, C., Choens, C., Paul, M., Stauffer, P., Guiltinan, E., Rahn, T., Otto, S., Davis, J., Eldridge, D., Rutqvist, J., Wu, Y., Hu, M., Chen, H., & Wang, J. (2024). *Brine Availability Test in Salt (BATS) FY24 Update Spent Fuel and High-Level Waste Disposition*.

Kuhlman, K., Mills, M., Jayne, R., Matteo, E., Herrick, C., Nemer, M., Xiong, Y., Choens, C., Paul, M., Downs, C., Stauffer, P., Boukhalfa, H., Guiltinan, E., Rahn, T., Otto, S., Davis, J., Eldridge, D., Stansberry, A., Rutqvist, J., … Wang, J. (2024). *Spent Fuel and Waste Disposition Brine Availability Test in Salt (BATS) FY23 Update*.

Laforce, T., Jayne, R., Leone, R., Mariner, P., & Stein, E. (2022). *Spent Fuel and Waste Disposition DECOVALEX-2023 Task F Specification*.

Mctigue, D. F. (1993). *Permeability and Hydraulic Diffusivity of Waste Isolation Pilot Plant Repository Salt Inferred from Small-Scale Brine Inflow Experiments*.

Ngo, D. T., & Pellet, F. L. (2018). Numerical modeling of thermally-induced fractures in a large rock salt mass. *Journal of Rock Mechanics and Geotechnical Engineering*, *10*(5), 844–855. https://doi.org/10.1016/j.jrmge.2018.04.008

Robertson, E. C. (1988). *Thermal Properties of Rocks*.

Schneider, M., Froggatt, A., Molin, A., Jobin, P., Johnstone, P., Judson, T., Kobayashi, Y., Koplow, D., Lyman, E., Wimmers, A. J., Vancouver, F. C., English, C., Copyeditor, L., Schneider, N., Hazemann, J., Ramana, M. V, Stier, S., & Von Hirschhausen, C. (2025). *The World Nuclear Industry Status Report 2024*. www.WorldNuclearReport.org

Staudtmeister, K., Zapf, D., Leuger, B., & Elend, M. (2017). Temperature Induced Fracturing of Rock Salt Mass. *Procedia Engineering*, *191*, 967–974. https://doi.org/10.1016/j.proeng.2017.05.268

Verhoef, E., Neeft, E., Bartol, J., Vuorio, M., Scholten, C., Buitenhuis, A., van der Veen, G., Chapman, N., & Mccombie, C. (2020). *Long-term Research Programme for Geological Disposal of Radioactive Waste*. www.covra.nl

Appendices

Appendix 1

Table with dimensions and function of each borehole mentioned in the experiments and models.

Dimensions Borehole (with HP being center of XZ system)

Borehole Name	Function	Diameter [m]	Length [m]	X-axis [m]	Z-axis [m]	Note
D	Ar Source	0.00533	4.582	0.021	0.202	Open space from 1.53 m to 4.582 m filled with pressurized Argon
E2	Sensor(s)	0.00533	5.7912	0.3	-0.493	-
F1	Sensor(s)	0.00533	5.4864	0.01	-0.191	-
F2	Sensor(s)	0.00533	9.144	-0.277	0.011	-
HP	Heater + Ar Sink	0.01219	3.8222	0	0	Heater location
T1	Sensor(s)	0.00533	5.4864	-0.961	0.006	-
T2	Sensor(s)	0.00533	5.4864	-0.658	0.011	-

Appendix 2

Table with dimensions and function of each sensor mentioned in the experiments and models.

Dimensions Sensors (with HP being center of XYZ system)

Sensor Name	Borehole	Depth [m]	X-axis [m]	Z-axis [m]	Distance to HP [m]
HE2RTD3	E2	2.972	0.294	-0.509	0.548
HF1TC2	F1	2.972	0.014	-0.234	0.193
HF2TC3	F2	2.972	-0.276	0.002	0.289
HP (center)	HP	2.972	0	0	0
T1TC10	T1	2.972	-0.969	-0.014	0.979
T1TC15	T1	4.572	-0.973	-0.025	1.875
T2TC10	T2	2.972	-0.675	0.022	0.688

Appendix 3

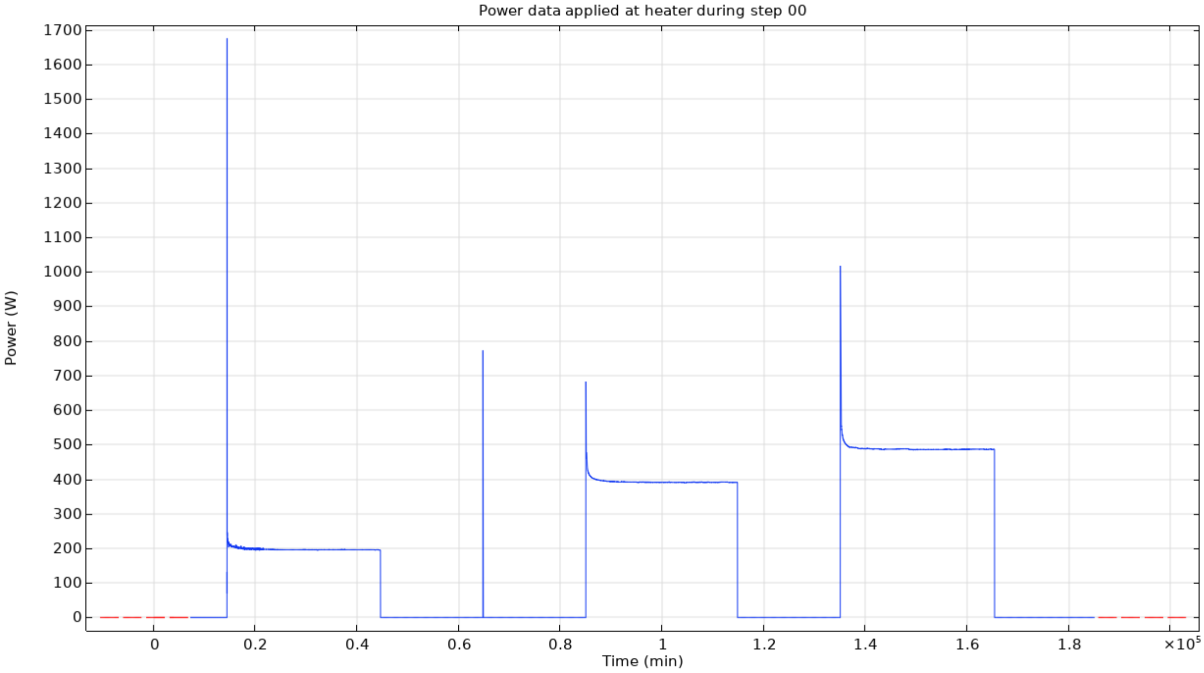

Appendix 4

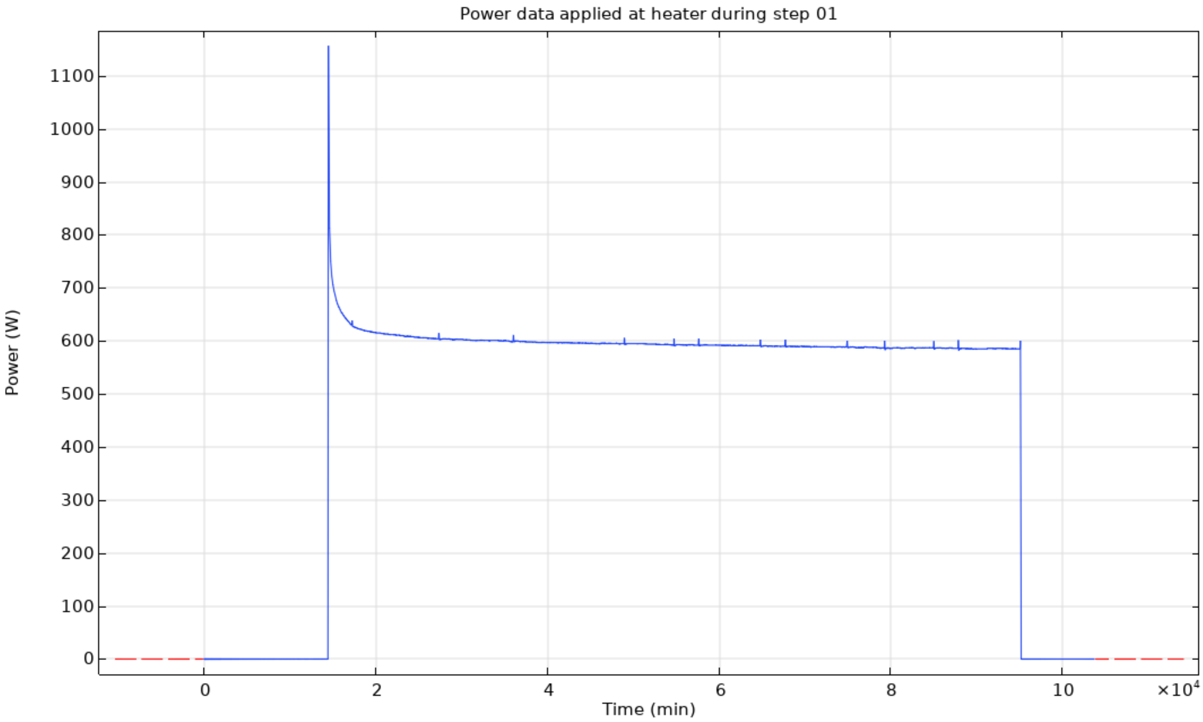

Appendix 5

Diagram with the experimental data of the temperature and specific heat capacity measured at the WIPP. The T-dependent specific heat capacity equation (with R^2) is plotted in the graph.

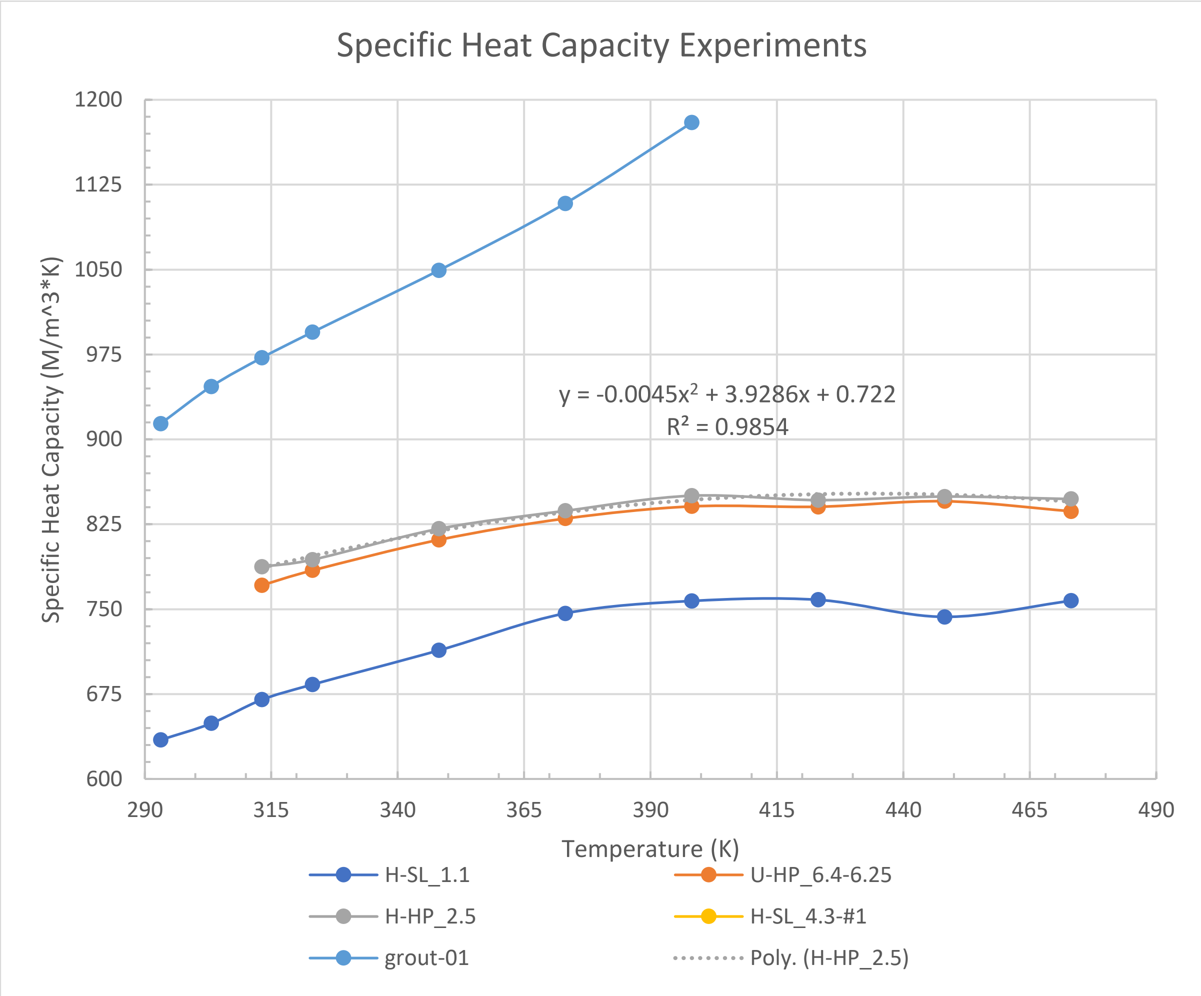

Appendix 6

Diagram with the experimental data of the temperature and thermal conductivity measured at the WIPP. The temperature-dependent thermal conductivity equation (with corresponding R^2) is plotted in the graph.

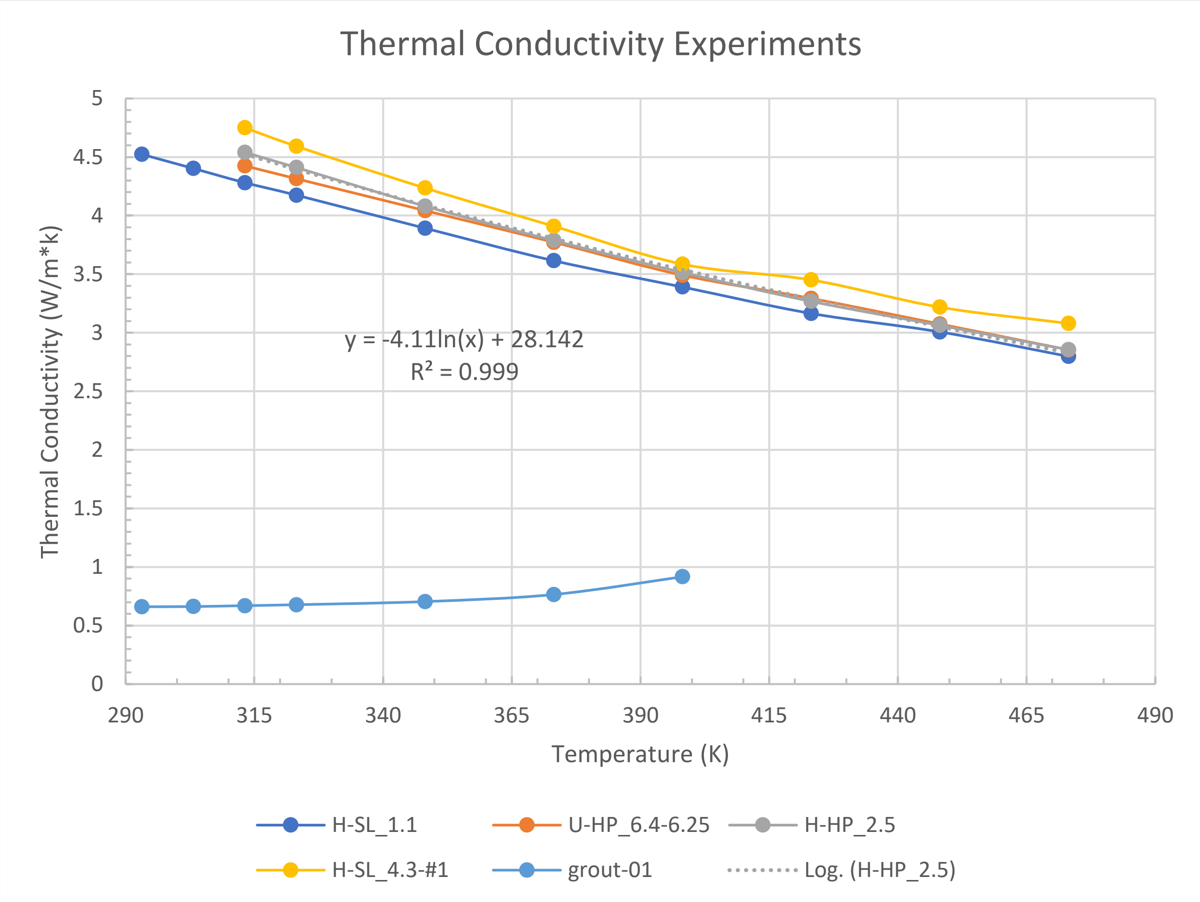

Appendix 7

During the temperature increase, the host rock will respond with thermal expansion. The volumetric expansion of the host rock will reduce the overall porosity and permeability of the heated rock body. Fractures below a certain size will also be closed, however the size will depend on the temperature that is reached. In my models, the fracture of interest is the one that connects the argon sink and source, resulting in 93% of the amount of argon to flow to the sink. This fracture is situated closest to the F1 sensor, the experimental values can therefore be used for calculations.

Gas flow through fractures primarily occurs due to Darcy flow (for larger fractures) or Knudsen diffusion (for very small fractures) (Ngo & Pellet, 2018). The transition between these flow regimes occurs at fracture apertures around 10 nm to 1 µm (Callister & Rethwisch, 2021). To completely block the flow of argon from the source to the sink, the fracture aperture should be ≤ 1µm. Calculating the fracture aperture to reduce to 1µm by purely thermal expansion can be done with using the thermal expansion equation shown below (Equation from Callister & Rethwisch, 2021). The L_0 will be the parameter of interest, with the thermal expansion coefficient of halite (α) having a value of $4.2*10^{-5}$ K^{-1}, ΔT at 45 K and ΔL is the required closure to reach ≤ 1 µm aperture.

$$L_0 = \frac{\Delta L}{1 - (2 * \alpha * \Delta T)}$$

Evaluating this equation would result in one fracture with an aperture of 1.004 µm that connects the source and the sink. But a network of fractures is also a possibility. It is important to remember that if the fracture is larger, additional effects like creep deformation and stress-induced closure may be required to seal it enough for gas migration to stop (Ngo & Pellet, 2018).